



Beneficial influence of EDTA on the structure and catalytic properties of sulfided NiMo/SBA-15 catalysts for hydrotreating of light gas oil

Sandeep Badoga ^a, K. Chandra Mouli ^a, Kapil K. Soni ^a, A.K. Dalai ^{a,*}, J. Adjaye ^b

^a *Catalysis and Chemical Reaction Engineering Laboratories, Department of Chemical Engineering, University of Saskatchewan, 57 Campus Drive, Saskatoon, SK, S7N 5A9, Canada*
^b *Syn crude Edmonton Research Centre, Edmonton, AB, T6N 1H4, Canada*

ARTICLE INFO

Article history:

Received 17 January 2012

Received in revised form 31 March 2012

Accepted 15 May 2012

Available online 29 May 2012

Key words:

EDTA

SBA-15

Sulfidation mechanism

XANES

LGO

Hydrotreating

ABSTRACT

SBA-15 supported NiMo hydrotreating catalysts with different EDTA/Ni molar ratio were prepared by incipient wetness impregnation method. Hydrotreating activities of these catalysts were studied with Athabasca bitumen derived light gas oil and comparison was done with NiMo/SBA-15 and NiMo/γ-Al₂O₃ catalysts. A beneficial effect of chelating ligand was seen in hydrotreating activity and 28% increase in HDS of LGO was found as compared to NiMo/γ-Al₂O₃ in the case of EDTA/Ni molar ratio 4. Detailed mechanistic aspect of interaction between support – EDTA (ethylene diamine tetraacetic acid), EDTA-metallic species, support – metal, metallic species – metallic species at different reaction conditions is studied at different process parameters by using different characterization techniques such as X-ray absorption near-edge structure (XANES), Fourier transform infrared spectroscopy (FTIR), HRTEM, XRD, Raman, temperature programmed reduction (TPR), ICP-MS, CO chemisorption and N₂ adsorption. A detailed scheme has been developed to explain the behavior of chelating agent in mesoporous SBA-15 supported catalysts. HRTEM results explain the high dispersion of Ni and MoS₂ active phases in sulfided state even though big crystallite of MoO₃ was seen in oxide state characterized by XRD and Raman spectra which explains role of EDTA in redistribution of active phases during sulfidation. XANES technique is used as predominant method for atomic level study of various structural changes in sulfided and oxide catalysts to find out the appropriate mechanism of the reaction. Characterization by XANES reveals that the presence of chelating agent delayed Ni²⁺ sulfidation which is main cause of improvement in HDS and HDN activity of the catalysts prepared in presence of organic chelates. Nickel sulfidation starts only when the EDTA–Ni complex decomposes and released nickel atoms move to the reactive edges of the MoS₂ to form a finely dispersed sulfide Ni–Mo–S type II active phase.

© 2012 Elsevier B.V. All rights reserved.

1. Introduction

Hydrotreating is the important process in refining industry for the removal of hetero-atoms such as sulfur, nitrogen and poisonous metals like vanadium, nickel, arsenic, from the crude oil [1]. The available petroleum reserves worldwide are heavier with substantial increase in sulfur and nitrogen contents. Additionally, the new environmental driven regulations require significant improvement in the quality of fuels [2]. As per current US EPA regulations, the sulfur content limits to 15 ppm. Consequently, hydrotreating catalysts with improved activity and selectivity are needed to meet the stricter sulfur specifications and quality of transportation fuels [3]. In recent years, the research is primarily focused on to increase the activity of catalyst and significant improvements have been achieved by changing the type of support materials, modifying the catalyst preparation methods, modification in active metal species,

using additives like fluorine, phosphorous and boron and use of chelating ligands [4–7].

Alumina supported sulfided Ni(Co)-Mo(W) catalysts were extensively used for hydrotreating of gas oil. During the past decade intensive efforts have been made in the direction of modification of catalysts by a variety of methods. Most of the studies described the influence of the support on the performance of hydrotreating catalysts. Different supports such as molecular sieves [8], amorphous and ordered mesoporous silica-aluminas [9], zirconia [10], titania [11], niobia [12], other mixed oxides [13,14], and zeolites [15,16] were used for hydrotreating. In recent years, the mesoporous silicate materials such as MCM-41, MCM-48, HMS, SBA-15, SBA-16, KIT-6, and FSM-16 [17–25] materials, with ordered pore structure, large pore diameters and higher surface areas than the γ-Al₂O₃ attracted widespread attention as new potential materials for the preparation of supported hydrotreating catalysts. There are several reports available on developing high performance supported hydrotreating catalysts on HMS, MCM-41 and SBA-15 materials. Principally, the HMS material prepared by a neutral template pathway offers certain advantages for the preparation of supported

* Corresponding author. Tel.: +1 306 966 4771; fax: +1 306 966 4777.

E-mail address: ajay.dalai@usask.ca (A.K. Dalai).

hydrotreating catalysts over the MCM-41 material that is synthesized by electro-statically template [26]. This advantage could be because the HMS material shows higher thermal and hydrothermal stability than the MCM-41 material. Unfortunately, the HMS material has low mechanical and thermal stability in comparison with the γ -Al₂O₃ [27]. Several solutions have been reported in open literature to enhance the stability of mesoporous materials. In this regard, SBA-15 material was synthesized having high thermal, hydrothermal and mechanical stability, and its textural properties are better than those of the HMS, MCM and traditional γ -alumina supports. Vradman et al. [28] reported the excellent performance of NiW/SBA-15 catalyst in the deep hydrodesulfurization (HDS) of petroleum feedstocks. Murali Dhar et al. [29] evaluated the catalytic activity of Mo/SBA-15 catalysts with 2–12 wt% Mo loadings, prepared by a standard incipient wetness impregnation method, in hydrotreating of model compounds. It was also observed that SBA-15-supported catalysts were 2–2.5 times more active compared to γ -Al₂O₃-supported catalyst.

It is also well established that the addition of chelating agents in the catalyst preparation is an effective way to improve catalytic activity. In 1986, a patent from Shell was the first to describe the use of chelating agents such as nitrilotriacetic acid (NTA) to improve the catalytic performances of CoMo and NiMo catalysts [30]. Many chelating ligands such as citric acid, glycol, nitrilotriacetic acid (NTA), ethylene diamine tetraacetic acid (EDTA), 1,2-cyclohexanediamine-tetraacetic acid (CyDTA) and ethylenediamine (EN) with hydrotreating catalyst were used and shown positive effect [31–34]. The chelating ligands are organic molecules that have two or more donor atoms, with which they can bind a metal cation and form a “chelate”. These agents favor the formation of stable complex with Ni or Co as compared to Mo and above 200 °C, these chelating ligands start to decompose to release Ni or Co. Thus, the strong interaction between chelating ligands and Ni ions leads to the sulfidation of these promoter metals at high temperatures. Once the temperature reaches to 200 °C, the complex decomposes and the Ni and Co atoms are released, they can sulfide and move to the edges of the already formed MoS₂ and create the Ni–Mo–S type II structures, which are the catalytically most active phases [35]. In the absence of chelating agents, a strong interaction between the support surface and molybdate species may occur, and polymolybdates may be dissociated to monomolybdates through such strong interactions. Extended X-ray absorption fine structure (EXAFS) spectrum of a CoMo/Al₂O₃ catalyst precursor prepared with chelating agents showed a strong Mo–Mo peak at 3.7 Å, indicating that most of the Mo is present as polymolybdate [36]. In the case of the catalyst prepared without a chelating agent, this peak was considerably smaller, indicating that polymolybdates decomposed to monomolybdate by the interaction with the support. Cattaneo et al. [37,38] also studied the effect of chelating agents on NiMo supported on silica and alumina. On silica, it appears that the formation of a complex between Ni and the chelating agent limits the carrier–promoter interaction and favors the Ni dispersion. No significant impact on Mo was observed unless high concentrations of chelating agent were used. Blanchard et al. [39] also thoroughly studied the influence of ethylenediamine on Mo and CoMo supported on alumina. Only the Co-promoted catalyst is more active when using ethylenediamine, whereas Mo/alumina is unchanged even at high Mo loading. Ethylenediamine molecule seems to inhibit the formation of cobalt molybdate and Co₃O₄ to increase the cobalt dispersion. To specify the effect of chelating agents on the sulfide slab structure, various studies were undertaken. Hensen et al. [40] as well as Okamoto et al. [41] used TEM spectroscopy analysis to study the effect of NTA on Mo/Al₂O₃ catalysts and found an increase of the length and stacking of the MoS₂ slabs with NTA loadings. For CoMo/Al₂O₃ catalysts, Gonzalez-Cortés et al. [42] showed that the addition of EDTA induces an

increase of the average slab length. These results are in contradiction with those reported by Hiroshima et al. [43], who used extended X-ray absorption fine structure in order to compare the dispersion of Mo on a CoMo/Al₂O₃ catalyst with or without NTA and concluded that Mo dispersion was independent of the presence of the chelating agent.

Hence, the literature shows some conflicts concerning the effect of chelating agent on the hydroprocessing activity. The objective of the present study is to determine the role of EDTA on the change of activity and functionalities of the catalysts more systematically at industrial conditions, and to relate these changes to the structure and concentration of active sites. In this current study the detailed mechanistic aspect of interaction between support – EDTA, EDTA–metallic species, support – metal, support–active phase, metallic species – metallic species at different reaction conditions is studied at different process parameters by using different characterization techniques such as XANES, FTIR, HRTEM, XRD, Raman, TPR, etc. A detailed scheme has been developed to represent all these interactions, sulfidation mechanism and genesis of active phase at different temperatures. XANES technique is used as predominant method for atomic level study of various structural changes in sulfided and oxide catalysts to find out the appropriate mechanism of the reaction. A set of EDTA–NiMo/SBA-15 catalysts with constant Ni and Mo contents and increasing EDTA amount was studied. The effect of EDTA on hydrotreating activity was tested using light gas oil as feedstock. The structure as well as the nature and amount of sulfide phase of the EDTA catalysts were characterized using CO chemisorption, HRTEM and XANES analysis.

2. Experimental

2.1. Support preparation

SBA-15 was synthesized by conventional hydrothermal method using poly(ethylene oxide)-block-poly(propylene oxide)-block-poly(ethylene oxide) (P123, average molecular weight 5800, EO₂₀PO₇₀EO₂₀) and tetraethoxysilane (TEOS) as template and silica source, respectively. This synthesis condition allows an easy and reproducible preparation of SBA-15 material with high yield. The gel composition is 20 SiO₂:0.16 P123:0.46 HCl. In a typical synthesis, 8 g of P123 was finely dispersed in 60 ml of water by stirring for 4 h at 40 °C. Then, 2 M HCl solution was added with stirring, which was continued for an hour. After getting a homogeneous solution, the silica source TEOS (18.2 ml) was added slowly with stirring. The gel mixture thus obtained was continuously stirred for another 24 h at 40 °C. Finally, the gel was transferred to Teflon bottle and autoclaved at 120 °C for 72 h. After cooling to room temperature, the solid product was filtered, washed and dried at 110 °C. The calcination of the as-synthesized materials was carried out at 500 °C with a heating rate of 3 °C/min in air for 6 h to remove the template molecules.

2.2. Catalyst preparation

All the catalysts were prepared on SBA-15 support by sequential pore filling impregnation procedure. The SBA-15 support was dried at 110 °C for 5 h prior to impregnation for removal of moisture. The Mo/SBA-15 catalyst (12.5 wt% Mo) was prepared by impregnation of a SBA-15 support with (NH₄)₆Mo₇O₂₄·4H₂O solution. The sample was dried at 100 °C for 6 h and calcined at 550 °C for 5 h to get Mo/SBA-15. This was used to prepare NiMo/SBA-15 catalysts having various EDTA/Ni ratios (0–2 molar ratio). NiMo/SBA-15 was prepared by impregnating 2.5 wt% of Ni on Mo/SBA-15 with nickel nitrate dissolved in an aqueous solution together with the chelating agent, EDTA. The impregnated powder was dried at 120 °C for 5 h.

NiMo/SBA-15 (EDTA/Ni = 0) was calcined at 550 °C for 6 h but calcination was not carried out for NiMo/SBA-15 (EDTA/Ni = 1 and 2) in order to avoid the decomposition of the complexes in the catalyst precursors. These samples were designated by CAT 0 (NiMoSBA-15; without chelating agent), CAT 1 (NiMo/SBA-15, EDTA/Ni molar ratio 1) and CAT 2 (NiMo/SBA15, EDTA/Ni molar ratio 2). For comparison purpose, NiMo/Al₂O₃ catalysts without chelating agent was prepared by impregnation of the Mo/Al₂O₃ with a nickel nitrate solution, drying, and finally calcining at 500 °C for 5 h with a heating rate of 3 °C/min.

2.3. Characterization

2.3.1. ICP-MS

The elemental compositions of the calcined NiMo/SBA-15 catalysts were measured by ICP-MS. A catalyst sample (0.1 g) was dissolved in concentrated hydrofluoric acid (48–51%) at a temperature of 100–150 °C for 3 days. After cooling, samples were further dissolved in concentrated HNO₃ to ensure the complete dissolution of the metals. The final solution was prepared using 0.2 N HNO₃ and analyzed with a mass spectrometer.

2.3.2. Measurement of N₂ adsorption–desorption isotherms

The BET surface area, pore volume, and pore size distribution of the samples were measured with a Micromeritics ASAP 2000 instrument using low temperature N₂ adsorption–desorption isotherms. Before measuring, the sample was degassed in vacuum at 200 °C. The surface area was computed from these isotherms using the multi-point Brunauer–Emmett–Teller (BET) method based on the adsorption data in the partial pressure P/P_0 range from 0.01 to 0.2. The value of 0.1620 nm² was taken for the cross-section of the physically adsorbed N₂ molecule. The mesopore volume was determined from the N₂ adsorbed at a $P/P_0 = 0.4$. The total pore volume was calculated from the amount of nitrogen adsorbed at $P/P_0 = 0.95$, assuming that adsorption on the external surface was negligible compared to adsorption in pores. The pore diameter and pore volume were determined using the (BJH) method. In all cases, correlation coefficients above 0.999 were obtained.

2.3.3. X-ray diffraction (XRD) analysis

The low-angle X-ray diffraction patterns of the samples were measured using a Bruker D8 Advance Powder diffractometer with a Ge monochromator producing a monochromatic CuK α radiation. The scanning was made from 1.5° to 10° with a 2θ step size of 0.02 and a step time of 2 s. In all cases, the generator was operated at 40 kV and 30 mA. To avoid the problem of illuminated areas at low 2θ angles, all samples were measured using the same sample holder. Broad angle powder X-ray diffraction patterns of all catalysts were recorded on a Rigaku diffractometer using CuK α radiation in the range 10–80° with a scan rate of 2°/min.

2.3.4. X-ray absorption near-edge structure (XANES) spectroscopy

The S K-edge, Ni K-edge and Mo LIII-edge XANES of the sulfided catalysts (three different temperatures) were obtained at the Soft X-ray Microanalysis Beamline (SXRMB) of the Canadian Light Source (CLS; Saskatoon, SK, Canada) using a Si (1 1 1) double crystal monochromator. CLS, a 2.9 GeV, third generation storage ring, presently operates with an injection current of 250 mA. The sample was dispersed on double-sided conducting carbon tapes under a dry nitrogen atmosphere, and the measurements were made in both total electron yield by recording the sample drain current and fluorescence yield using a PGT single element Si(Li) drift detector. The XANES spectra were normalized to incident photon flux and to unity at the maximum intensity of each spectrum.

2.3.5. Raman spectroscopy

The Raman spectra were obtained using a Renishaw Raman InVia Microscope (Spectra-Physics model 163), operated at the argon ion laser operating at wavelength of 514 nm. The laser spot size was approximately 1–2 μ m with a power of 3.6 mW. The wavenumber accuracy was ± 2 cm^{−1}.

2.3.6. Temperature programmed reduction (TPR)

H₂-temperature programmed reduction (H₂-TPR) of the catalysts was carried out using TPD/TPR-2720 Micromeritics (USA) instrument for analyzing the nature of reducible metal species present in the samples. A 50 mg sample in a quartz tube was purged with He at 400 °C for 1 h to remove impurities on the surface of the sample. After the sample was cooled to room temperature in flowing He, TPR was carried out using 3% H₂/N₂ (v/v) mixture at a flow rate of 30 ml/min. The heating rate was 10 °C/min from room temperature to 1000 °C. TPR profiles were recorded with a thermal conductivity detector.

2.3.7. CO chemisorption

The Micromeritics ASAP 2020 Chemisorption system was used to measure the carbon monoxide uptake on the oxide catalysts. Prior to the CO chemisorptions measurement, sample was evacuated and backfilled with helium at 35 °C and then evacuated at 110 °C for 60 min. The sample was then heated to 350 °C @ 10 °C/min in the presence of hydrogen and was maintained at 350 °C for 2 h. The sample was cooled down to 35 °C and then evacuated until the static pressure remained less than 1.3×10^{-5} Pa. The analysis (chemisorptions) was performed by passing pulses of CO over the sample to measure the total CO uptake at 35 °C. The following expression was used to calculate the percentage metal dispersion of the active metal available for interaction with the adsorbate.

$$\%M_{\text{Disp}} = \frac{1}{22414^{\circ}} \times \frac{V * SF_{\text{CALC}}}{(\text{weight fraction of Mo}/W_{\text{ATOMIC,Mo}}) + (\text{weight fraction of Ni}/W_{\text{ATOMIC,Ni}})}$$

where $\%M_{\text{Disp}}$ is metal dispersion (%), V is volume intercept derived from the best line fit to the volume differences between the selected points of the first analysis and the repeat analysis (cm³/g STP), SF_{CALC} is calculated stoichiometry factor.

2.3.8. Transmission electron microscopy (TEM)

The morphological features of the support and catalysts were studied from electron micrographs obtained with a JEOL 2011 scanning transmission electron microscope. The powder samples were grounded softly in an agate mortar and dispersed in heptane in an ultrasonic bath for several minutes. A few drops were then deposited on 200 mesh copper grids covered with a holey carbon film. The electron micrographs were recorded in electron negative films and in a digital PC system attached to the electron microscope.

2.3.9. Fourier transform infrared spectroscopy (FTIR)

The framework vibration of supported catalysts was examined by FTIR spectroscopy. KBr pellet technique was employed to obtain infrared spectra of the samples at room temperature. The spectra were retrieved in the wavenumber range of 400–2000 cm^{−1} with a resolution of 4 cm^{−1} by an infrared spectrometer type JASCO FTIR 4100.

2.4. Catalytic activity

Hydrotreating experiments were performed in a trickle bed reactor under typical industrial conditions. The KLGO derived from

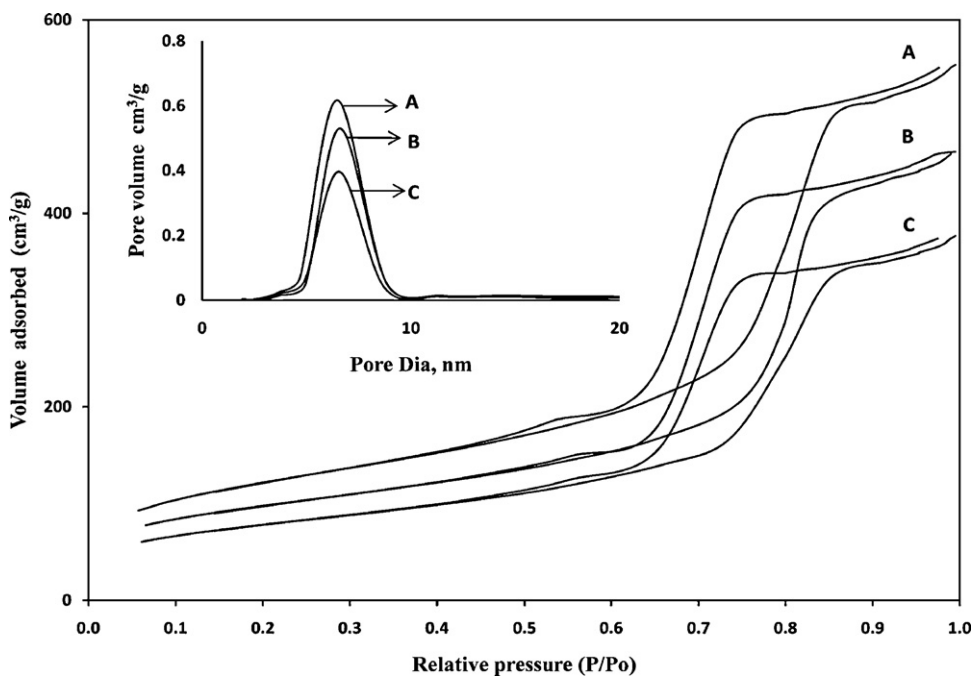


Fig. 1. N_2 adsorption–desorption isotherm and BJH pore size distribution of NiMo/SBA-15 catalysts (A) CAT 0, (B) CAT 1, (C) CAT 2.

Athabasca bitumen was used as a feed for the hydrotreating studies. KLGO is a complex combination of hydrocarbons from the distillation of the products from a thermal cracking process (fluid coker). It consists of hydrocarbons having carbon numbers predominantly in the range of C_{11} – C_{28} and boiling in the range of 200–450 °C with specific gravity of 0.95 at 20 °C and contains 0.24 and 2.3 wt% of nitrogen and sulfur, respectively. The high pressure reaction set up used in this study simulates the process that takes place in industrial hydrotreaters. The system consists of liquid and gas feeding sections, a high pressure reactor, a heater with temperature controller for precisely controlling the temperature of the catalyst bed, a scrubber for removing the ammonium sulfide from the reaction products, and a high pressure gas–liquid separator. The length and internal diameter of the reactor were 240 and 14 mm, respectively. The details of catalyst loading into the reactor are described elsewhere [44]. Typically, the catalyst bed, approximately 10.5 cm long, was packed with 5 cm³ of catalyst (2.0 g) and 12 cm³ of 90 mesh silicon carbide.

The catalyst was sulfided by injecting sulfidation solution containing 2.9 vol% of butanethiol in straight run atmospheric gas oil at a pressure and temperature of 8.8 MPa and 193 °C, respectively, for 24 h. The flow rate of the sulfiding solution was 5 ml/min. The H₂ flow rate was kept at a rate corresponding to H₂/sulfidation solution ratio of 600 ml/ml. The temperature of the reactor was increased to 343 °C and maintained for another 24 h. Following sulfidation, the catalyst was precoked (stabilized) with LGO for 5 days at a temperature of 370 °C, pressure of 8.8 MPa, and LHSV of 2.0 h⁻¹. After precoking, HDN and HDS activities of the catalysts were studied at three different temperatures of 370, 350, and 330 °C using KLGO for 3 days at each temperature. The pressure, H₂/feed ratio and LHSV were maintained constant at 8.8 MPa, 600 ml/ml and 2.0 h⁻¹, respectively. The products were collected at 12 h intervals and the products stripped with nitrogen for removing the dissolved ammonia and hydrogen sulfide. The total nitrogen content of the liquid product was measured by combustion/chemiluminescence technique following ASTM D4629 method, and the sulfur content was measured using combustion/fluorescence technique following ASTM D5463 method. Both sulfur and nitrogen were analyzed in an Antek 9000 NS analyzer. The instrumental error in N and S analysis was 3%.

3. Results and discussion

3.1. N_2 Adsorption–desorption isotherms

The textural characteristics of catalysts were examined by BET surface area and BJH pore size distribution. N_2 Adsorption–desorption isotherms of NiMo/SBA-15 catalysts with and without chelating agents are given in Fig. 1. All the catalyst samples exhibit type IV isotherms with a H₁ type hysteresis loop, which correspond to hexagonal pore system of SBA-15 and supported catalysts. It is clear from Fig. 1 that shape of hysteresis loop is maintained after metal loading, indicating that structure of the material is intact after Mo, Ni and EDTA loading. The decrease in the height of hysteresis loops indicates the loss of pore volume, due to the filling of pores by Ni, Mo and EDTA species. The inserted narrow pore size distribution graph in Fig. 1 indicates the average pore diameter of SBA-15 supported catalysts is around 6.7 nm.

The numerical data of BET and BJH results are summarized in Table 1 which indicates the decrease in the surface area and pore volume upon loading of nickel and molybdenum oxide which further reduces with EDTA loading. The specific surface area and total pore volume decreases from 441 m²/g and 0.85 cc/g in CAT 0 to 282 m²/g and 0.57 cc/g in CAT 2, respectively whereas, the average pore diameter remains same (around 6.7 nm) for CAT 0, CAT 1 and CAT 2.

This could be explained by substantial blocking of pore openings by large MoO₃ crystallites (as discussed in Section 3.2) and Ni–EDTA complex. Fig. 1 shows that SBA-15 has ordered

Table 1
Textual properties of SBA-15 supported catalysts.

Catalyst	BET Surface area (m ² /g)	Pore Volume (cm ³ /g)	Avg. pore dia. (nm)
CAT 0: NiMo/SBA15, Without EDTA	441	0.85	6.6
CAT 1: NiMo/SBA15, EDTA/Ni molar ratio 1	351	0.71	6.9
CAT 2: NiMo/SBA15, EDTA/Ni molar ratio 2	282	0.57	6.7

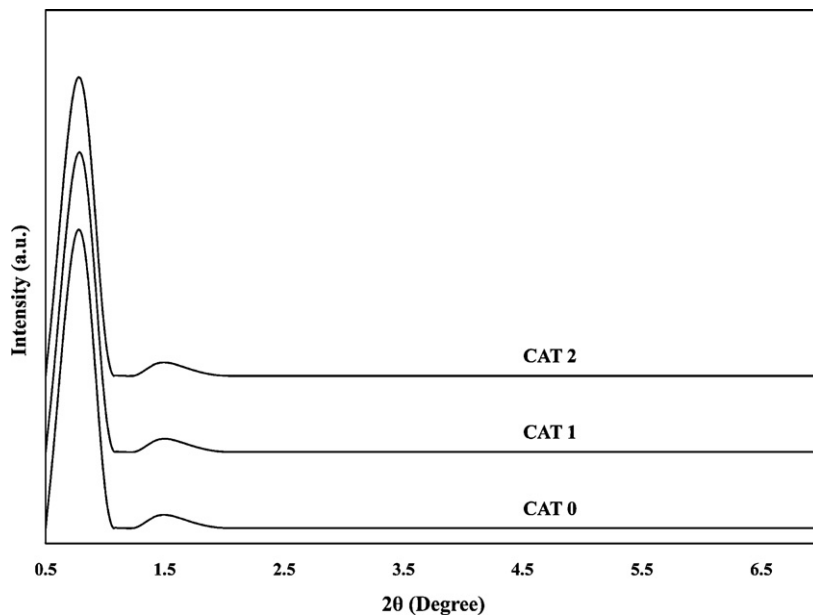


Fig. 2. Low angle XRD pattern of NiMo/SBA-15 catalysts (A) CAT 0, (B) CAT 1, (C) CAT 2.

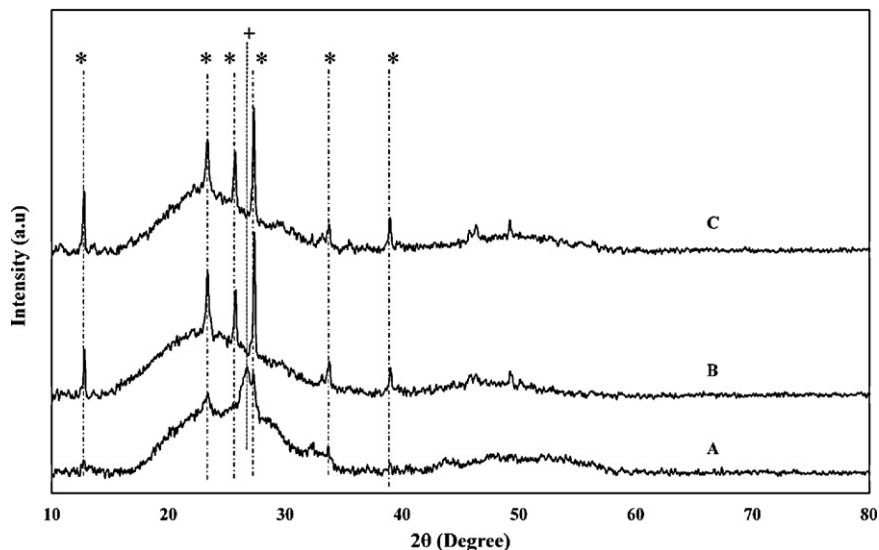


Fig. 3. Wide angle XRD pattern of NiMo/SBA-15 catalysts (A) CAT 0, (B) CAT 1, (C) CAT 2, (*) represents MoO_3 peaks and (+) represents $\beta\text{-NiMoO}_4$ peaks.

hexagonal pore structure with narrow pore size distribution. Thus, the blocking of pore openings by MoO_3 crystallites reduces the total surface area and volume, not the average pore diameter. However, large MoO_3 crystallites break down and re-disperse during sulfidation (Scheme 2) and make pores accessible for the reaction. The re-dispersion is probably more uniform due to narrow pore size distribution and ordered hexagonal pore structure of SBA-15 catalyst.

3.2. X-ray diffraction

The XRD measurements were carried out to study the mesoporous structure of the supported catalysts. The crystalline phases of the calcined catalysts can also be obtained by this technique. The low angle XRD pattern of NiMo catalysts supported on SBA-15 with different EDTA/Ni ratios are shown in Fig. 2 in the interval between the 2θ values of 0.5–10. The small-angle XRD pattern of the calcined SBA-15 supported catalyst materials should show

three well-resolved characteristic of SBA-15 materials. These peaks are indexable as d_{100} , d_{110} and d_{200} reflections associated with the $p6mm$ symmetry of the hexagonal ordered pore structure. Although the two peaks due to d_{110} and d_{200} have been merged and one broader peak is observed instead of two small peaks. It is clear from Fig. 2 that the intensity of all three peaks in all catalysts are almost same indicating the intact hexagonal structure of material after NiMo and EDTA loadings.

Powder wide angle XRD patterns for NiMo/SBA-15 catalysts with different EDTA loading are shown in Fig. 3. It can be seen from Fig. 3 that a broad peak between 20° and 30° can be observed for all samples which corresponds to amorphous silica material. Diffraction peaks due to the orthorhombic MoO_3 crystalline phase (JCPDS card 35–609) is observed in all catalysts. It is clear from figure that dispersion of MoO_3 reduces with increasing the amount of EDTA in catalysts. The intensity of sharp peaks at 12.7° , 23.3° , 25.7° and 27.3° is higher for CAT 1 and CAT 2 catalysts compared to CAT 0 catalysts indicate the presence of large MoO_3 crystallites and poor

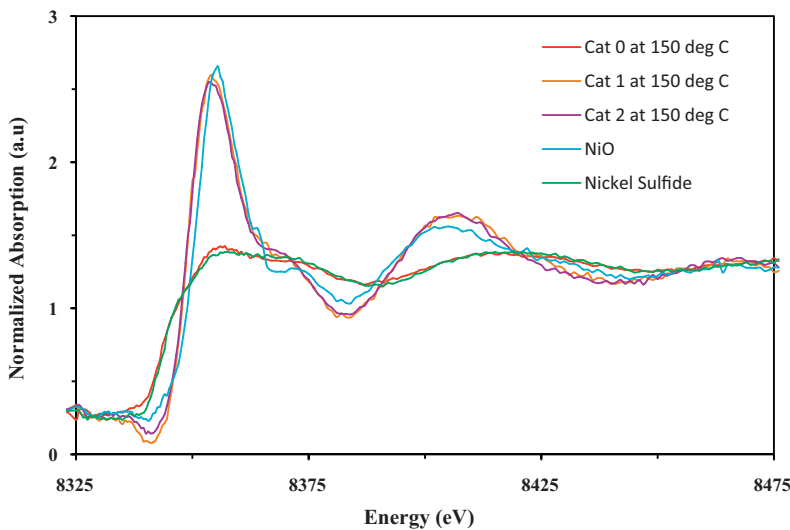


Fig. 4. XANES spectra of sulfided Ni K-edge of (A) CAT 0 at 150 °C, (B) CAT 1 at 150 °C, (C) CAT 2 at 150 °C, (D) NiO, (E) nickel sulfide.

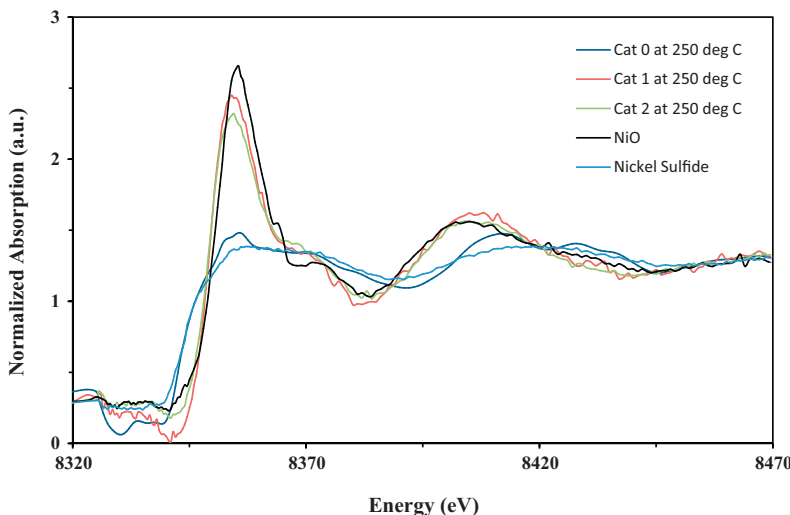


Fig. 5. XANES spectra of Ni K-edge of (A) CAT 0 at 250 °C, (B) CAT 1 at 250 °C, (C) CAT 2 at 250 °C, (D) NiO, (E) nickel sulfide.

dispersion in CAT 1 and CAT 2 catalysts. In the case of CAT 0, an additional peak of β -NiMoO₄ phase is observed at 26.7° [45].

The approximate crystallite size for MoO₃ is calculated using Scherrer's equation,

$$d_{\text{avg-size}} = \frac{0.8 * \lambda}{\beta * \text{Cos} \theta}$$

where $d_{\text{avg-size}}$ is the average crystal size, λ the X-ray wavelength, β the FWHM (full width at half max) of the reflection peak and θ is the Bragg angle [46]. The MoO₃ crystallite size for CAT 0 is 15 nm and for CAT 1 and CAT 2 catalysts, it is almost same and equals to 25 nm. This size is large than the internal pore diameter of SBA-15. Therefore, these crystallites sit on the pore mouth of the support and block some pores as shown in Scheme 2. In CAT 0 catalyst, the presence of nickel significantly improves the dispersion of Mo species [47], whereas, in case of catalysts with EDTA, nickel forms complex with EDTA and does not play any role in dispersion of MoO₃, that leads to bigger MoO₃ crystal size in CAT 1 and CAT 2 as compared to CAT 0 and results in the sharp crystalline peaks in CAT 1 and CAT 2 catalysts. The metal dispersion

of CAT 1 and CAT 2 will improve significantly during sulfidation of molybdenum as discussed in CO chemisorptions and HRTEM section.

3.3. XANES

3.3.1. Ni K-edge analysis

Figs. 4–6 shows the Ni K edge XANES spectra for catalyst CAT 0, CAT 1 and CAT 2 sulfided at three different temperatures 150, 250 and 350 °C along with the reference spectra for nickel oxide (octahedral geometry) and nickel sulfide (a mix of different sulfides of nickel viz., pyrite shaped NiS₂, tetrahedral Ni₃S₂ or octahedral NiS). Ni K-edge for NiO shows an intense peak at 8355 eV due to dipole allowed 1s to 4p transition, which is a property of transition metals and with reduction of nickel oxide to nickel sulfide the peak becomes less intense and broad as seen in Figs. 4–6 for reference peak of nickel sulfide [48,49]. This change in peak intensity and broadness also confirms that the octahedral coordination of nickel in nickel oxide is changed to tetrahedral or mixture of octahedral O_h, tetrahedral T_h and other lower coordination's during the

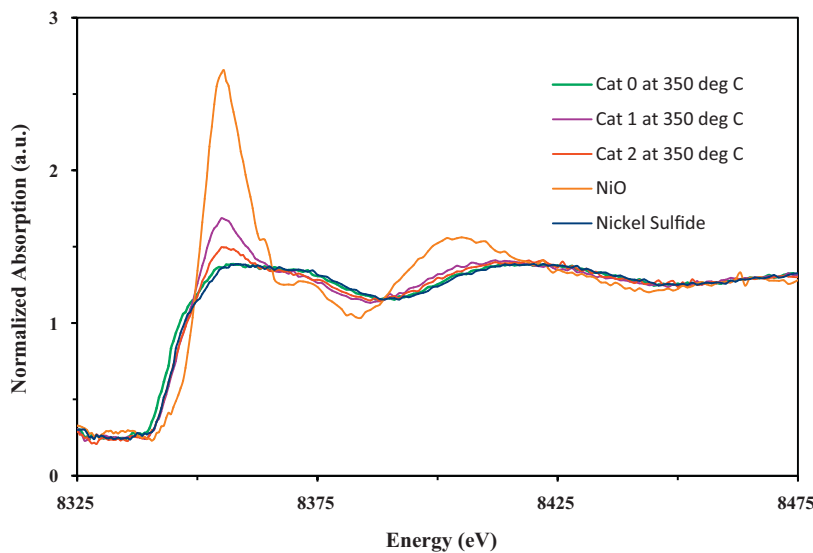


Fig. 6. XANES spectra of sulfided Ni K-edge of (A) CAT 0 at 350 °C, (B) CAT 1 at 350 °C, (C) CAT 2 at 350 °C, (D) NiO, (E) nickel sulfide.

formation of nickel sulfide [50]. Pre-edge spectra actually give more idea about the oxidation state and coordination geometry. Sharp pre-edge peak signifies the Td symmetry and small pre-edge peak signifies the octahedral symmetry. But for Td symmetry the pre-edge peak intensity decrease as we move from Fe to Cu in periodic table and is absent for Zn. This decrease in intensity is due to progressive filling of the 3d band. It indicates that the pre-edge peak intensity for Oh and Td is almost same for Ni [51]. Therefore, it is difficult to conclude anything from pre-edge in this case. It is clear from Fig. 4 that at 150 °C, Ni in CAT 0 catalysts is fully sulfided as it resembles the XANES for reference nickel sulfide, whereas in CAT 1 and CAT 2 the Ni is still in oxide state. It shows that EDTA helps in delaying the sulfidation of nickel. The sulfidation in catalyst CAT 1 and CAT 2 starts at 250 °C (see Fig. 5) because the EDTA complex becomes unstable at around 220 °C and it releases the Ni which starts to sulfide. Fig. 6 shows that at 350 °C there is complete sulfidation of Ni. It can be seen in Fig. 6 that the Ni K-edge peak for CAT 1 and CAT 2 is sharp whereas for CAT 0 it is broad. The sharp peak represents the octahedral geometry whereas broad peak is for tetrahedral geometry. As said Ni sulfides in different coordination geometries and the octahedral NiS are most favored for hydrotreating [52], it can be concluded from Ni K-edge spectra that with EDTA more of octahedral NiS is formed. Hence EDTA not only delays the sulfidation but also helps in favorable sulfidation of nickel.

3.3.2. Mo LIII-edge

Mo LIII-edge is studied for oxide and sulfide states to get the better understanding of EDTA effects on Mo coordination and dispersion. Fig. 7 shows the Mo LIII-edge spectra for catalysts CAT 0, CAT 1 and CAT 2 at oxide states along with reference spectra for MoO₃ (octahedral symmetry) and alpha-NiMoO₄ (octahedral). In all Mo LIII-edges there is a white line at around 2525 eV corresponding to 2p to 4d electronic transitions, and the splitting in LIII-edge is because of the ligand field splitting of the d orbitals. As per Rodriguez et al. [53] splitting of Mo 4d orbital is smaller in a tetrahedral co-ordination as compared to octahedral coordination. If the most intense peak of split peak is at higher energy the geometry is tetrahedral otherwise it is octahedral. So it can be assumed from XANES Mo LIII-edge that reference MoO₃ (splitting distance 3 eV) and NiMoO₄ (α -phase) are in octahedral geometry. It can also be seen in Fig. 7 that the splitting between 4d orbitals in Mo LIII-edge of CAT 0 is smaller (1.6 eV peak to peak distance) and also the intensity of split peaks is almost same. It signifies that Mo is in

mixture of octahedral MoO₃, alpha NiMoO₄ and β -NiMoO₄ tetrahedral symmetry. But with increasing the EDTA loading from CAT 1 to CAT 2 the splitting increase (2.5–2.9 eV) and resembles more with octahedral MoO₃ peaks (splitting distance 3 eV), which is quite obvious because EDTA forms complex with Ni and very less Ni is available to form NiMoO₄ phases. In case of higher EDTA loading (CAT 2), less Ni is available which consequently increases the presence of MoO₃ octahedral phase. Similar types of results have been found in XRD and RAMAN spectra also (see Sections 3.2 and 3.4).

Mo LIII-edge for sulfided catalysts CAT 0, CAT 1 and CAT 2 along with reference for MoS₂ and MoO₃ is shown in Figs. 8 and 9. Mo in MoO₃ is in +6 oxidation state whereas in MoS₂ it is in +4 oxidation state, and that is the reason for shifting in peak energies by 3 eV between two spectra of MoS₂ and MoO₃ [54]. In the case of CAT 1 and CAT 2 at 150 °C the Mo LIII-edge is at similar energy to that of MoO₃, which reflects that sulfidation of MoO₃ does not start at 150 °C. Whereas for CAT 0 Mo LIII-edge is between the energy of MoO₃ and MoS₂ LIII-edge (1.2 eV below that of MoO₃). It signifies that Mo is in between +4 and +6 oxidation state. This indicates that Mo in NiMoO₄ gets partially reduced upon sulfidation of NiMoO₄. It does not happen in case of catalyst with EDTA because there is almost no NiMoO₄ phase. It is shown in Fig. 8 that as the temperature reaches to 250 °C, the Mo LIII-edge of all three catalysts is at the energy very close to Mo LIII-edge of MoS₂, which reflects that sulfidation of MoO₃ is started which completes at 350 °C.

It can be concluded from XANES Mo L III edge and Ni K-edge that EDTA helps in formation of more MoO₃ phase which starts to sulfide at around 250 °C, and it also delays the Ni sulfidation to around 250 °C. The sulfidation of both Mo and Ni at around same temperature will help in formation of more type II NiMoS active phases. This result is also supported by HRTEM analysis.

3.3.3. S K-edge spectra

The sulfur K-edge for CAT 0, CAT 1 and CAT 2 is shown in Figs. 10 and 11 along with the reference spectra for MoS₂. The intense white line at 2471 eV followed by additional feature at 2479 eV characterizes the spectra of MoS₂. The similar spectra are reported for NiS [55]. In other words it can be said that this intense white line signifies sulfur in -2 oxidation state, S²⁻. Chaturvedi et al. [54] reported that the peak at 2482 eV is because of sulfate ion SO₄²⁻ (sulfur in +6 oxidation state), which is formed during partial sulfidation of alpha and β -NiMoO₄. At 150 °C it can be seen in Fig. 10 that, CAT 0 shows a S²⁻ peak

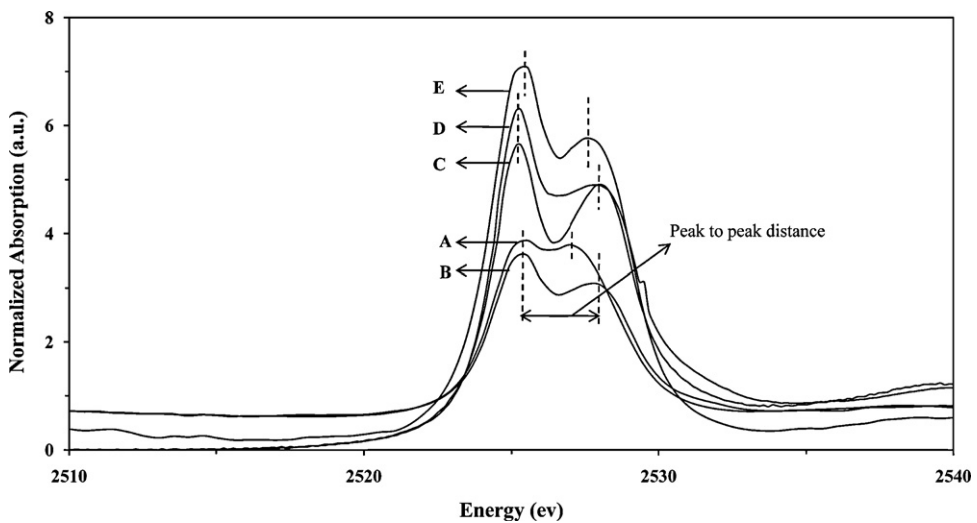


Fig. 7. XANES spectra Mo LIII-edge of (A) CAT 0 oxide, (B) CAT 1 oxide, (C) CAT 2 oxide, (D) MoO₃, (E) NiMoO₄.

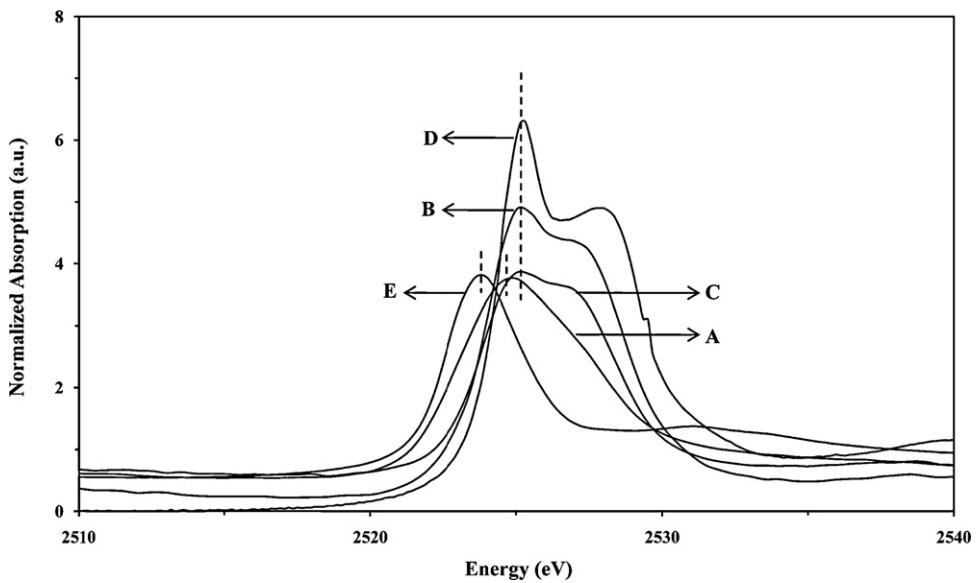


Fig. 8. XANES spectra of sulfided Mo LIII-edge of (A) CAT 0 at 150 °C, (B) CAT 1 at 150 °C, (C) CAT 2 at 150 °C, (D) MoO₃, (E) MoS₂.

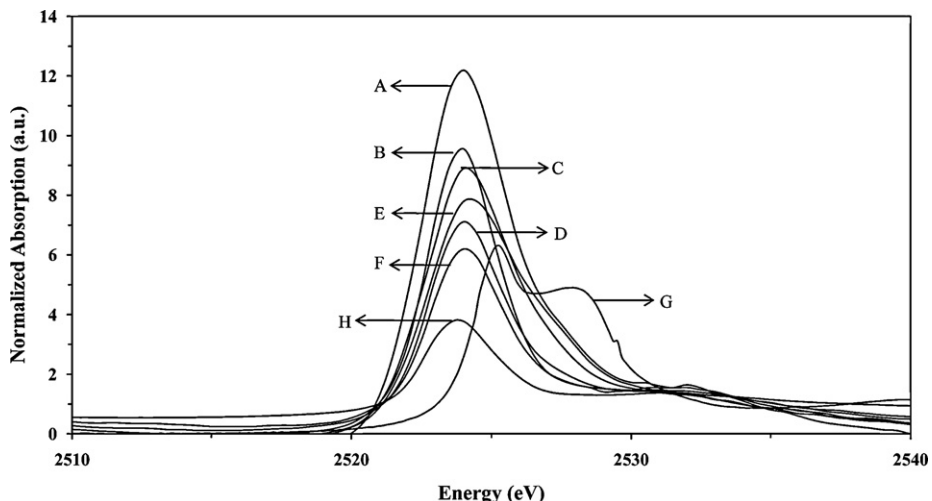


Fig. 9. XANES spectra of sulfided Mo LIII-edge of (A) CAT 0 at 250 °C, (B) CAT 0 at 350 °C, (C) CAT 1 at 250 °C, (D) CAT 1 at 350 °C, (E) CAT 2 at 250 °C, (F) CAT 2 at 350 °C, (G) MoO₃, (H) MoS₂.

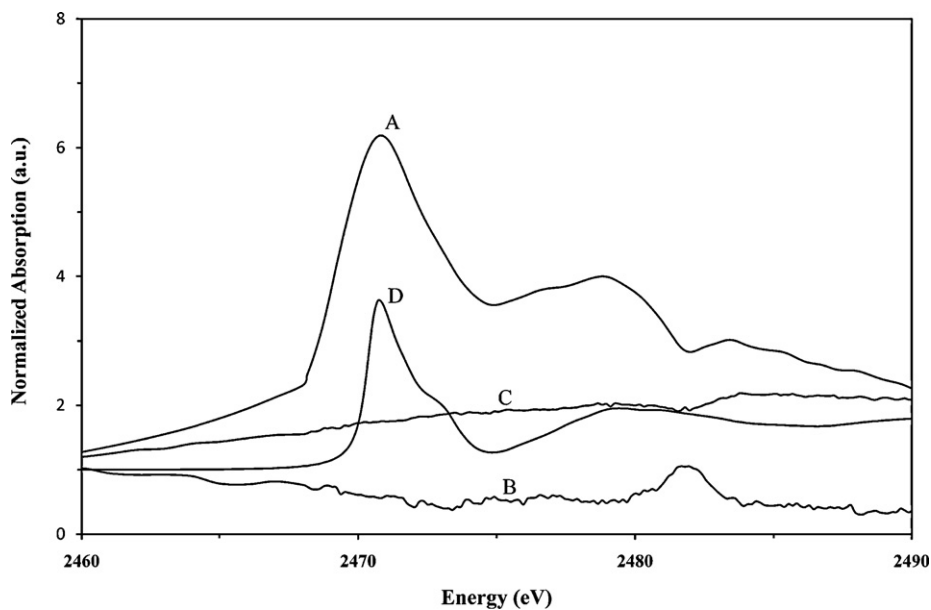


Fig. 10. XANES spectra of S K-edge of (A) CAT 0 at 150 °C, (B) CAT 1 at 150 °C, (C) CAT 2 at 150 °C, (D) MoS₂.

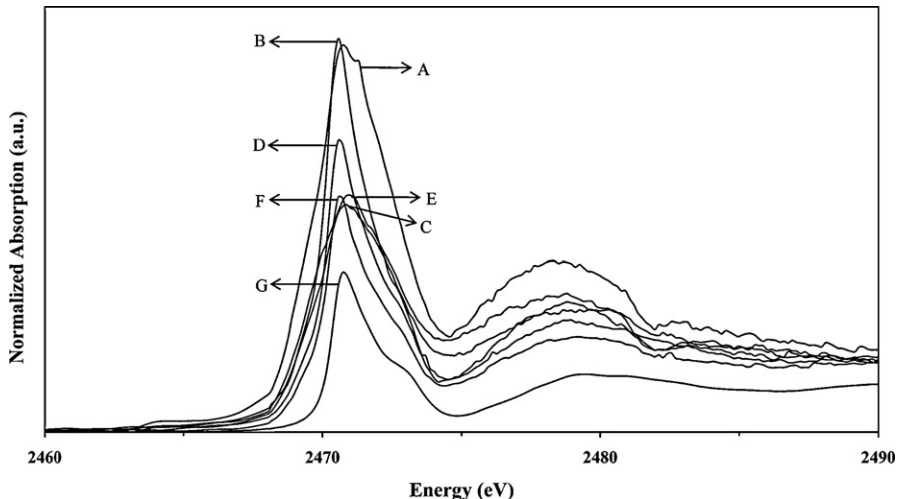


Fig. 11. XANES spectra of sulfided S K-edge of (A) CAT 0 at 250 °C, (B) CAT 0 at 350 °C, (C) CAT 1 at 250 °C, (D) CAT 1 at 350 °C, (E) CAT 2 at 250 °C, (F) CAT 2 at 350 °C, (G) MoS₂.

at 2471 eV. And as per Mo LIII-edge Fig. 9 Mo starts sulfiding at around 250 °C so this peak is only because of sulfidation of nickel. On contrary to this, there is no S²⁻ peak in CAT 1 and CAT 2 at 150 °C, because EDTA complexes with Ni to prevent it from sulfiding. There is small sulfate peak at 2482 eV in CAT 1, which signifies the presence of some amount of alpha or β-NiMoO₄ which is partially sulfided [54]. But in CAT 2 there is no such peak. It can be inferred that EDTA to Ni molar ratio 1 is not sufficient to complex all Ni present and as we go higher in molar ratio the free Ni availability becomes negligible and no NiMoO₄ phase is found and hence no sulfate peak. With increase in temperature to 250–350 °C, Fig. 11, all three catalysts show a S²⁻ peak corresponding to MoS₂ and NiS which indicates the complete sulfidation.

The structural information provided by XANES, Ni K-edge, S K-edge and Mo LIII-edge, confirm that EDTA helps in delaying the Ni sulfidation temperature to 250 °C. EDTA also helps in formation of more octahedral MoO₃ phase, which is favorable during sulfidation as both NiO and MoO₃ starts sulfiding at same temperatures. This will help in formation of more type II Ni–Mo–S phases. S K-edge also reveals that EDTA to Ni molar ratio 1 is not enough to

encapsulate all Ni with EDTA because of this remaining Ni, either in NiO or NiMoO₄ still sulfides at lower temperatures and this is not desired. Higher EDTA to Ni molar ratio is desired for better results.

3.4. Raman analysis

To determine the nature of the oxide phases present on the support surface Raman spectroscopy was employed. The Raman spectra of CAT 0, CAT 1 and CAT 2 catalysts are shown in Fig. 12. All spectra exhibit peaks at 155.0, 289.5, 664.0, 818.0, 994.0 cm⁻¹ and these peaks represent MoO₃ crystallites on supported catalysts [56]. It can be seen that with increase in EDTA loading intense peaks corresponding to MoO₃ are observed which indicates the increase in MoO₃ crystallites size from CAT 0 to CAT 2 and implies poor dispersion in CAT 2 as compared to CAT 0 and CAT 1. The Raman vibrations at 959 cm⁻¹ in CAT 0 corresponds to the presence of the β-NiMoO₄ phase which was also proved by wide angle XRD pattern [57]. The impregnation of Ni and Mo on SBA-15 support was done in presence of water. The support surface in this condition is basic and negatively charged which facilitate the molybdate ions to interact more favorably with the positively charged Ni ions. This will cause

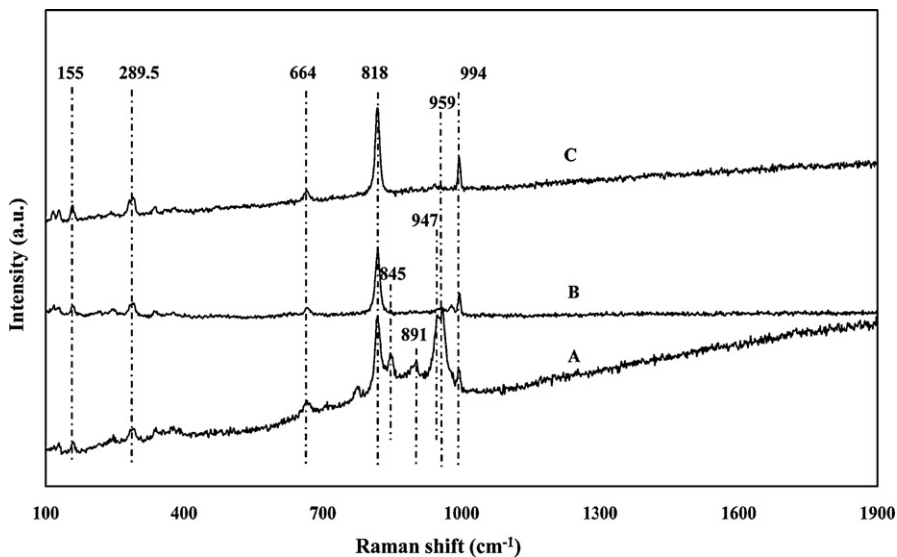


Fig. 12. Raman Spectra of NiMo/SBA-15 catalysts (A) CAT 0, (B) CAT 1, (C) CAT 2.

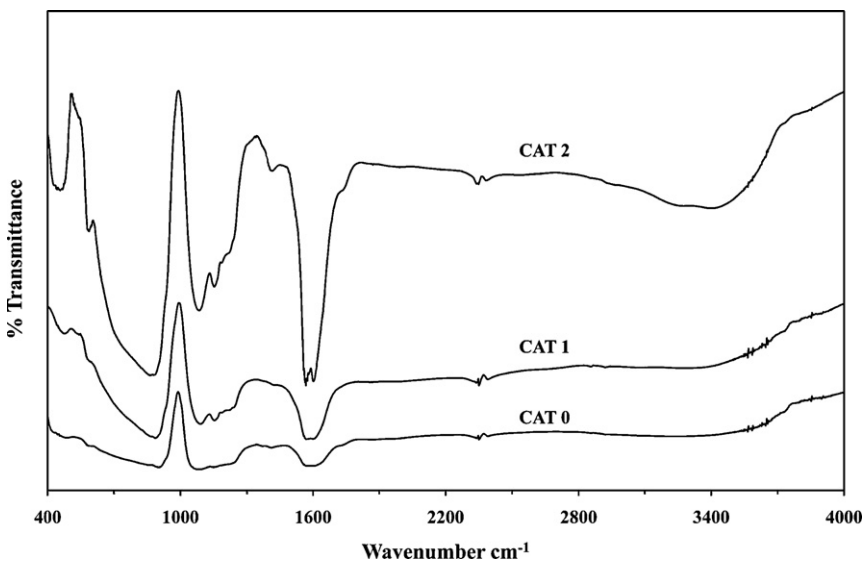


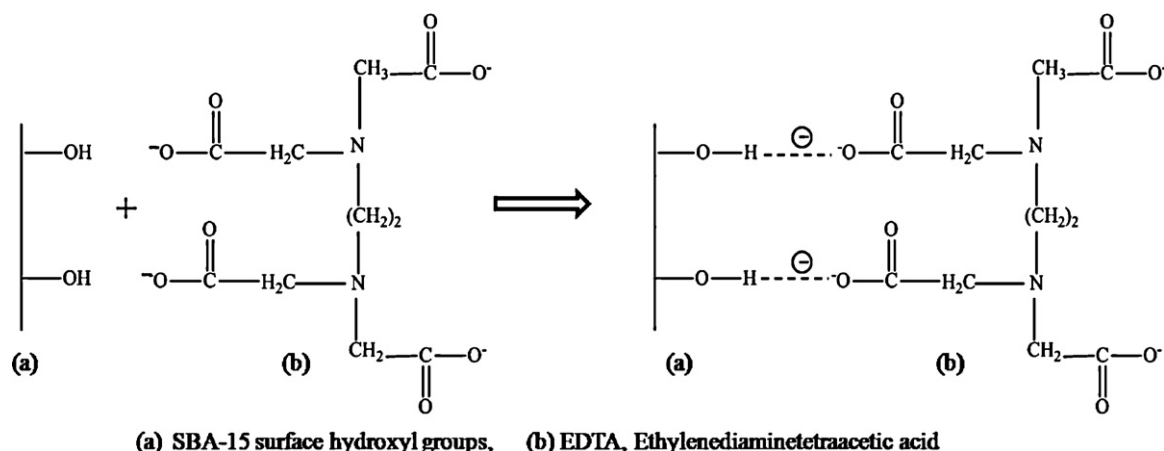
Fig. 13. FTIR spectra of CAT 0, CAT 1 and CAT 2.

the formation of β -NiMoO₄ phases when the catalyst is calcined. In EDTA loaded catalysts, EDTA forms the complex with available Ni species and inhibits the formation of NiMoO₄ phase which explains the absence of this peak at 959 cm⁻¹. Peaks at 947 and 891 cm⁻¹ indicate the symmetric stretching of the Mo=O bond in bridged or two-dimensional polymeric forms of octahedrally coordinated Mo oxide species, which could be attributed to Mo₇O₂₄⁻⁶ species [58]. Such Mo oxide species are considered to interact weakly on the supports, resulting in higher reducibility and activity in HDS and HDN. Presence of MoO₃ crystallites is not desired in oxide state of catalyst because it represents poor dispersion but as discussed in Section 3.2, that the presence of chelating agent EDTA, will increase the dispersion of MoO₃ crystallites during sulfidation which results in higher activity.

3.5. Fourier transform infrared spectroscopy

Fig. 13 displays FTIR spectra of CAT 0, CAT 1 and CAT 2. All the catalysts show bands at 3450–3650 cm⁻¹ and 1574–1600 cm⁻¹ which are attributed to the stretching and bending vibrations of the

surface silanol groups [59]. Intensity of these bands increases from CAT 0 to CAT 1 to CAT 2 indicating the presence of more Si-OH groups. It implies that with increase in EDTA concentration there is an increase in formation of polymolybdates and decrease in dispersion from CAT 0 to CAT 2. The same result is presented by XRD and RAMAN analysis also. The typical Si-O-Si bands around 925, 1050–1275 and 455 cm⁻¹ associated with the formation of a condensed silica network are present in all the catalysts. Additionally, catalyst with EDTA shows intense peak at 1725, 1575–1605 and 1410 cm⁻¹ as compared to CAT 0. These bands are mainly due to interactions of the chelate carboxyls with inorganic hydroxyl groups present on the surface of SBA-15 [60–62]. The band at 1605 cm⁻¹ are due to asymmetric stretching of COO⁻ group present in EDTA and the band at 1410 is because of symmetric stretching of COO⁻. The peak at 1725 cm⁻¹ is because of C=O stretching vibration [61]. The increase in intensity of these bands from CAT 1 to CAT 2 is because of increase in concentration of EDTA. FTIR spectra reveal that there is interaction between EDTA and support material. Possible interaction of surface hydroxyl groups of SBA-15 with EDTA is being presented in Scheme 1 [62].



Scheme 1. Interaction of SBA-15 surface OH group with EDTA.

3.6. Temperature programmed reduction

TPR patterns and trends in the reducibility of Mo in CAT 0, CAT 1 and CAT 2 catalysts are presented in Fig. 14. CAT 0 shows main reduction peak at 530 °C and it could be assigned to the reduction of Mo⁶⁺ species in polymolybdate structures to Mo⁴⁺ species. In CAT 1, the presence of EDTA favors the formation of large crystallites of easily reducible octahedral MoO₃ (as shown by XRD and RAMAN Sections 3.2 and 3.4) which helps in reducing metal support interaction and results in low temperature reduction of molybdenum at 485 °C.

TPR profile of molybdenum reduction in CAT 2 (Fig. 14) covers the temperature region 400–580 °C starting from 400 °C and reaching a maximum at 582 °C. The peak reduction temperature of Mo in CAT 2 is 52 °C more than that of catalyst without EDTA (CAT 0). This is because of the fact that CAT 2 contains double the amount of EDTA as compared to CAT 1 and some of the excess EDTA forms complex with molybdenum oxide, the same is reported by Sun et al. [5,63]. EDTA-Mo complex is stable and reductive decomposition of [(MoO₃)₂EDTA] complex requires high temperatures resulting in peak reduction temperature of 582 °C in CAT 2.

3.7. CO chemisorption

Table 2 shows the metal dispersion, surface area and crystal size measured by CO chemisorptions for NiMo/SBA-15 (with various EDTA concentrations) catalysts. Prior to CO chemisorption the catalyst was reduced with hydrogen at 350 °C and the metal dispersion was based on CO uptake by the reduced catalyst. It can be seen that there is increase in quantity of CO adsorbed with increase in EDTA loading from 151 μmol/g in CAT 0 to 333 μmol/g in CAT 2. This rise in absorption is because of increase in metallic surface area per gram of catalyst. The percentage metal dispersion follows the order CAT 2 > CAT 1 > CAT 0. As shown in Table 2, the metal crystallite size measured by CO chemisorptions for CAT 0 catalyst is 14.5 nm and it is in accordance with the value of 15 nm size obtained from Scherrer's equation for CAT 0, but in the case of CAT 1 and CAT 2, it is different than the crystallite size, obtained from Scherrer's equation. In catalysts with EDTA, Ni forms complex with EDTA and this complex are stable up to 200 °C. During CO chemisorption, the pretreatment takes place at 350 °C and at this temperature Ni-EDTA complex in CAT 1 and CAT 2 catalysts decomposes and releases nickel. This Nickel eventually helps in

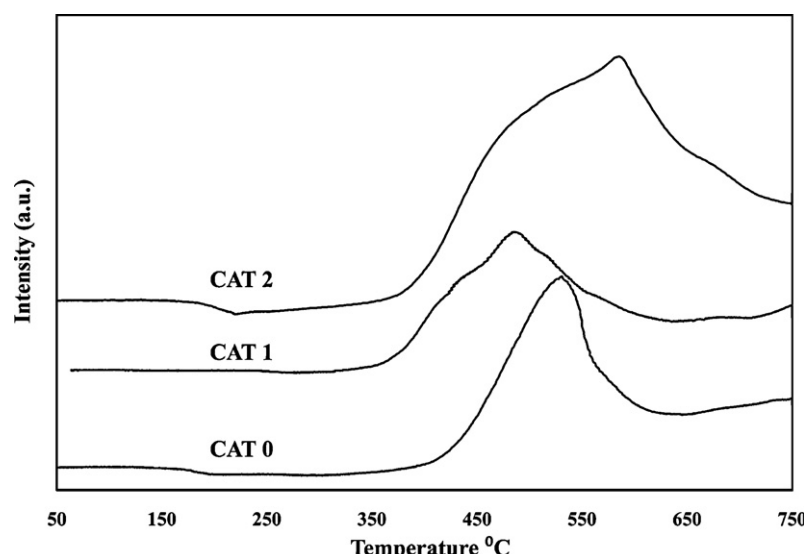
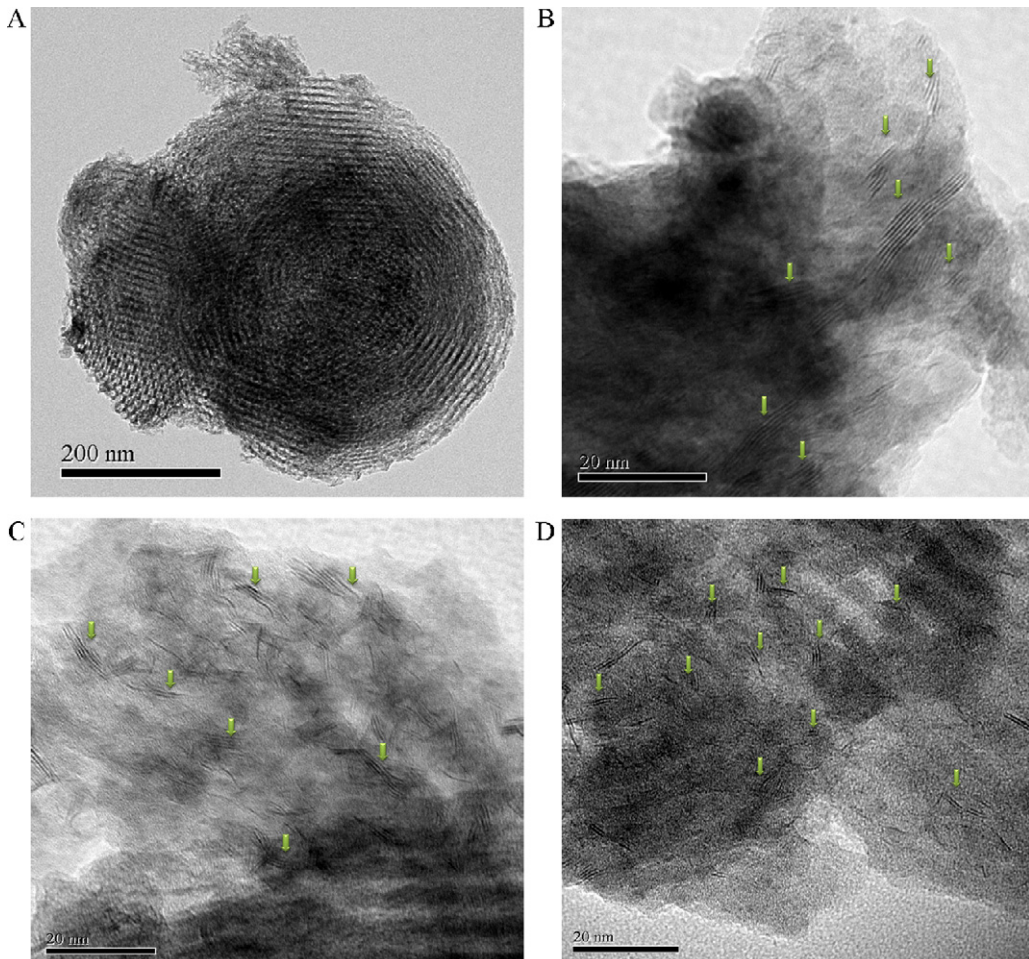


Fig. 14. TPR profile of CAT 0, CAT 1 and CAT 2.

Table 2

Chemical composition and CO uptake of SBA-15 supported catalysts.

Catalyst	ICP-MS		Metal dispersion (%)	Metallic surface area (m ² /g, of sample)	Metallic surface area (m ² /g, of metal)	Crystallite size (nm)	CO adsorbed (μmol/g)
	Ni (wt%)	Mo (wt%)					
CAT 0	2.38	11.5	8.5	6.5	41.7	14.5	151
CAT 1	2.40	11.4	14.2	10.8	69.5	8.7	252
CAT 2	2.35	11.6	18.7	14.3	91.9	6.5	333

**Fig. 15.** Distribution of MoS₂ slabs in SBA-15 supported catalysts (A) CAT 1 at resolution of 200 nm, (B) CAT 0 @ resolution 20 nm, (C) CAT 1 @ resolution 20 nm, (D) CAT 2 @ resolution 20 nm.

better dispersion of MoO₃ species resulting in lower crystallite size of 6–8 nm (Table 2). Whereas, during XRD all the catalysts remain in oxide state and the presence of stable EDTA–Ni complex in CAT 1 and CAT 2 leads to formation of bigger MoO₃ crystallites, which is shown by XRD pattern and Scherrer's equation for CAT 1 and CAT 2. This explains the same crystallite size measurement by CO Chemisorption and Scherrerr's equation for CAT 0 and different in the case of CAT 1 and CAT 2.

3.8. HRTEM

To study in depth the effect of EDTA on structure and dispersion of active components on the supports, HRTEM characterization was carried out for the sulfided catalysts. HRTEM micrographs of the sulfided catalysts reflect the changes in the morphology of MoS₂ with increasing EDTA loading (Fig. 15). The HRTEM micrographs shown in Fig. 15A are at resolution of 200 nm and the hexagonal pore structure of SBA-15 template can be seen whereas, Fig. 15B–D

was at resolution of 20 nm so the hexagonal pore structures of SBA-15 are not clearly visible. The typical fringes due to MoS₂ crystallites with 6.1 Å interplanar distances were observed from micrographs of all sulfided catalysts. The slab length and stacking degree distribution for the same catalysts can be seen in Fig. 16. It is clear from Fig. 16 that incorporation of EDTA in catalysts has significant impact on slab length and heights which results in improved catalytic activity. Catalyst without EDTA (CAT 0, Fig. 15B) shows the length of MoS₂ crystallites between 2 and 10 nm with average length of 6.2 nm (Table 3) and stacking from 2 to 6 layers with average stacking of 4.5 layers. Higher number of MoS₂ stacks (up to six MoS₂ layers or more) hampers the dispersion of active phase. With catalyst CAT 1, there is reduction in slab length as well as in stacking degree of MoS₂ particles (Fig. 15C and Fig. 13). As shown in Table 3, average stack length of 4.8 nm with average stacking of 2.9 layers is observed for CAT 1. With further increase in EDTA concentrations, short MoS₂ particles were formed predominantly as seen in case of sulfided CAT 2 catalysts (Fig. 15D) with average

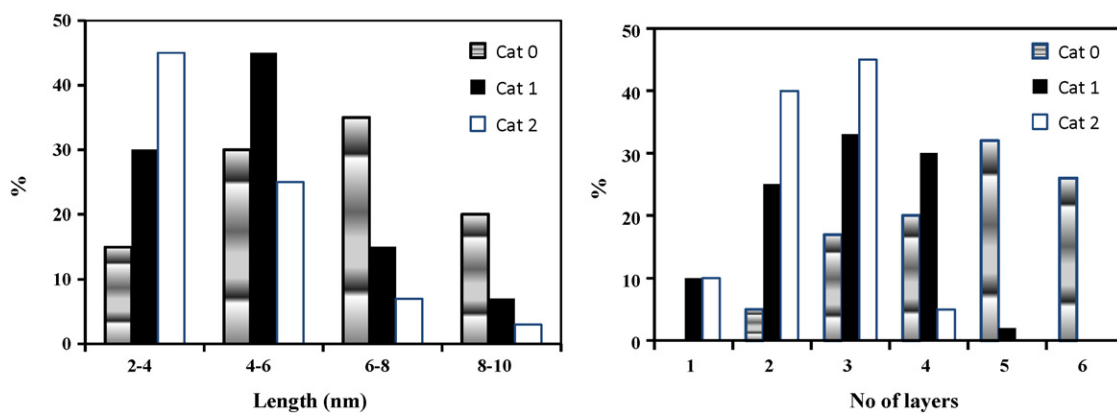
Fig. 16. Length and layer stacking distribution of MoS₂ slabs in the catalysts.

Table 3

Average length (L) and number (N) of the stacking layers.

Catalyst	Average length (nm)	Average stacking (no. of layers)
CAT 0	6.2	4.57
CAT 1	4.8	2.89
CAT 2	3.3	2.45

length of 3.3 nm and average stacking of 2.4 layers. HRTEM analysis of catalysts shown in Figs. 15 and 16 clearly indicates that the EDTA addition has resulted in better dispersion and more homogeneous distribution of MoS₂ crystallites.

It was observed from XRD that the average metal crystallite size of oxide catalysts (CAT 1 and CAT 2) is large (~25 nm) which is reduced to 6.5–8.7 nm during CO chemisorption measurements. The decrease in crystal size is because of the redistribution of metal crystals at 350 °C, when they are reduced under hydrogen environment prior to CO adsorption. Similar reduction conditions existed during sulfidation (second paragraph, Section 2.4). It was observed from CO chemisorption that the average size of metal crystallites in CAT 0 is 14.5 nm and for CAT 1 is 8.7 nm. This size is more than the SBA-15 pore size (Table 1), so the fraction of MoO₃ and then MoS₂ after sulfidation is on the surface of SBA-15. In CAT 2 the crystal size was measured as 6.5 nm and pore size was 6.7 nm so the probability of presence of MoS₂ on the surface of CAT 2 is less as compared to CAT 0 and CAT 1. The presence of MoS₂ slabs on the external surface of SBA-15 in CAT 1 and CAT 0 signifies the presence of randomly oriented MoS₂ slabs in the HRTEM micrographs for CAT 1 and CAT 0 as compared to more organized MoS₂ slabs in HRTEM micrographs of CAT2 (Fig. 15). This may be one of the reasons for enhanced activity of CAT 2 over CAT 0 and CAT 1.

3.9. Catalytic activity

In this study, the HDN and HDS activities, expressed as percent conversion, were measured using synthesized NiMo/SBA-15 catalysts with and without chelating agents. For comparison, the activity study of NiMo/γ-Al₂O₃ was also carried out. To achieve steady-state activity, the catalysts were stabilized by precoking using KLGO for 5 days. Initial HDN and HDS activities of these catalysts are high which shows the presence of high number of active sites at the initial stage of hydrotreating. The N and S conversions of the KLGO catalysts decreased with time on stream and reached steady-state after 3 days, probably due to coking of the acidic sites.

After precoking, the steady-state activities of all prepared catalysts were studied using the same feed at reaction temperatures. The activity was studied for 72 h at each temperature and samples were collected after every 12 h. The average N and S conversions

Table 4

HDN and HDS activities of NiMo/γ-Al₂O₃ and CAT 0–5 catalysts with KLGO at 370 °C (catalyst = 5 cm³, P = 8.8 MPa, LHSV = 2 h⁻¹ and H₂/oil ratio = 600 (v/v)).

Catalyst	%Sulfur conversion	%Nitrogen conversion
NiMo/γ-Al ₂ O ₃	68	42
CAT 0	70	24
CAT 1	75	27
CAT 2	82	34
CAT 3	85	40
CAT 4	88	47
CAT 5	84	35

of the last four samples at reaction temperature of 370 °C are shown in Table 4. The activity results show that NiMo/SBA-15 (EDTA) catalysts show higher HDS catalytic activities compared to reference catalysts under similar reaction conditions. The N-S conversion confirms the following order for HDS activity: CAT 2 > CAT 1 > CAT 0 > NiMo/γ-Al₂O₃ and following order for HDN activity CAT 2 > NiMo/γ-Al₂O₃ > CAT 1 > CAT 0. This higher hydrotreating activity of CAT 2 catalysts is due to (i) presence of more amount EDTA which forms complex with almost all Ni present and delays the Ni sulfidation temperature, (ii) better dispersion of Ni and Mo active species, (as seen in CO chemisorptions) and (iii) formation of more dispersed type II NiMoS active phases. Higher HDS activity of SBA-15 supported catalyst as compared to NiMo/γ-Al₂O₃ is due to large surface area, pore diameter, ordered structure and narrow pore size distribution in SBA-15. It helps in easy diffusion of larger feed molecules leading to higher hydrotreating activity. Also, the weak metal support interactions in NiMo/SBA-15 as compared to NiMo/γ-alumina will enhance the formation of polymolybdates. These are easy to sulfide, leading to the formation of more type II NiMoS active phases responsible for higher HDS activity. Low HDN conversions on SBA-15 supported catalysts as compared to NiMo/γ-Al₂O₃ catalysts are explained below.

Acidity and hydrogenation are the two important characteristics of catalyst which affect the hydrodenitrogenation reaction. First about acidity, in previous work reported by our group [56,64], it was observed that total acidity of NiMo/SBA-15 catalyst is less than that of NiMo/γ-Al₂O₃. Results from the pyridine FTIR of catalysts NiMo/γ-Al₂O₃ and NiMo/SBA-15 showed that the peak at 1540 cm⁻¹, indicating the Brønsted acid sites is missing in latter case. Li et al. [65] performed NH₃-TPD to measure the acid strength of the catalyst and they observed weak acidity of SBA-15 as compared to γ-Al₂O₃ supported catalysts. It was observed that HDN activity for catalyst having low acidity and less number of Brønsted sites is less than that for catalysts having large number of Brønsted sites. In our case, the weak acidic properties of SBA-15 may be

responsible for its low HDN conversion as compared to NiMo/γ-Al₂O₃.

Secondly, the hydrodenitrogenation reaction follows the hydrogenation pathway followed by C–N bond scission. This implies that better the hydrogenation activity better will be the HDN reactions. In order for hydrogenation of aromatic nitrogen containing compound to occur these molecules should be adsorbed by their π aromatic electrons and the adsorption will be favorable if there is optimum length and stacking of Ni–Mo–S slabs (type II NiMoS active phase) [66]. In our case, HRTEM analysis has shown that CAT 2 has optimum length and stacking of MoS₂ slabs as compared to CAT 0 and CAT 1 and follows the order CAT 2 > CAT 1 > CAT 0. This implies that hydrogenation activity and hydrodenitrogenation activity should also follow the same order. The results of catalytic activity studies support the above fact and there is an increase in HDN activity of CAT 2 by 41% as compared to CAT 0 (Table 4).

It can be concluded that the beneficial effect of EDTA on hydrotreating activity is mainly because of delay in Ni-sulfidation temperature to the point where molybdenum is already sulfided. Similar beneficial effects of EDTA on hydrotreating activity of γ-alumina supported catalysts have been previously reported by our group [44]. But the extent of effect of EDTA on hydrotreating activity does depend on type of support material due to variation in support properties including acidity and metal support interactions. The percentage increase in HDS activity for γ-alumina supported catalysts with and without EDTA is less as compared to that for silica (SBA-15) supported counterpart because of high metal support interaction in former case [34,67]. In the presence of EDTA, the weak metal support interactions lead to the formation of polymolybdates which are easy to sulfide and responsible for the formation of multiple stacking, type II NiMoS phases. Whereas, the strong metal support interaction in case of γ-alumina results in the formation of tetrahedral aluminum molybdenum complex which is difficult to sulfide. However, the HDN conversions for γ-alumina supported NiMo-EDTA catalyst is more as compared to that on NiMo/SBA-15-EDTA catalyst because of the higher acidity of γ-alumina support, which makes alumina as a better support.

Based on the results from different characterization techniques such as XANES, XRD, RAMAN, FTIR, CO chemisorptions and HRTEM, the sulfidation mechanism and the role of chelating ligand can be represented by Scheme 2. Scheme 2A shows that CAT 0 in oxide state has well dispersed MoO₃, NiO and α, β-NiMoO₄ inside the pores. The MoO₃ groups are attached to the surface of SBA-15 via OH group. XRD and CO chemisorptions data show that the average MoO₃ crystallite size is 14.5 nm which is higher than that of SBA-15 pore size. Thus fraction of MoO₃ crystallites will be on the external surface of silica SBA-15 as shown in schematic for CAT 0 oxide (see Scheme 2A). During sulfidation at 150 °C, and beyond, the large MoO₃ crystallites break down into small crystals and majority of them move inside the pores. Also, at 150 °C nickel oxides convert to mixture of nickel sulfides such as heazlewoodite Ni₃S₂, hexagonal shaped NiS and cubic structured NiS₂, whereas the MoO₃ remains unreacted as the sulfidation of Mo starts above 150 °C [5,37]. The same conclusion can be derived from Ni K-edge and Mo LIII-edge in XANES spectra. With increase in temperature the MoO₃ begins to sulfide and at temperature of 250 °C most of the MoO₃ converts to MoS₂. Further increase in temperature helps in the formation of multiple layers of MoS₂ slabs as shown in CAT 0 sulfide at 350 °C in Scheme 2A. (Fig. 15 B). At these conditions nickel is already in sulfide phase, which prevent the movement of Ni atoms to the corners and edges of MoS₂ slab and resulted in less numbers of Ni–Mo–S active phases formation. This is the reason behind the lesser activity of CAT 0 even though it has multiple stacking of MoS₂ slab.

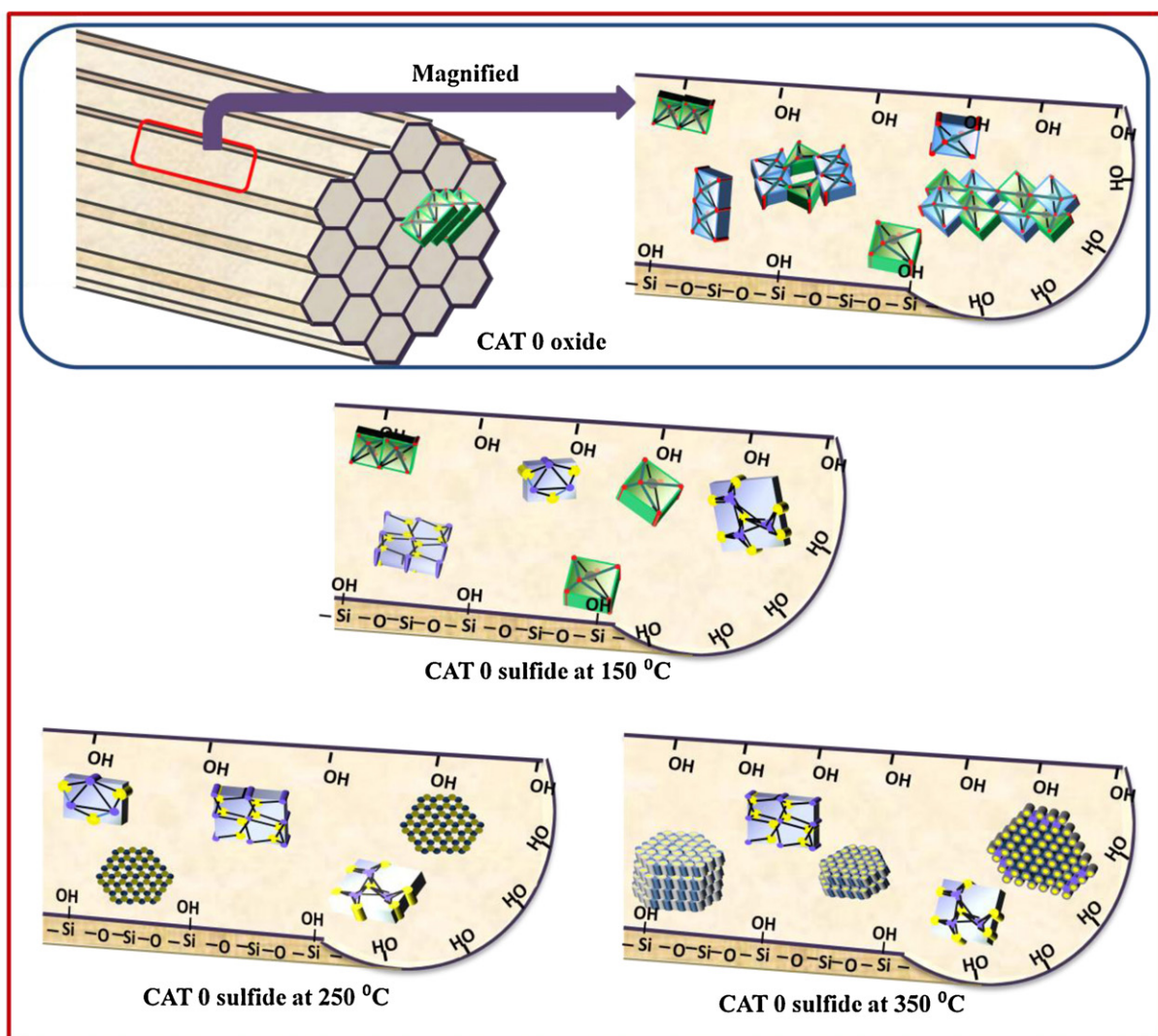
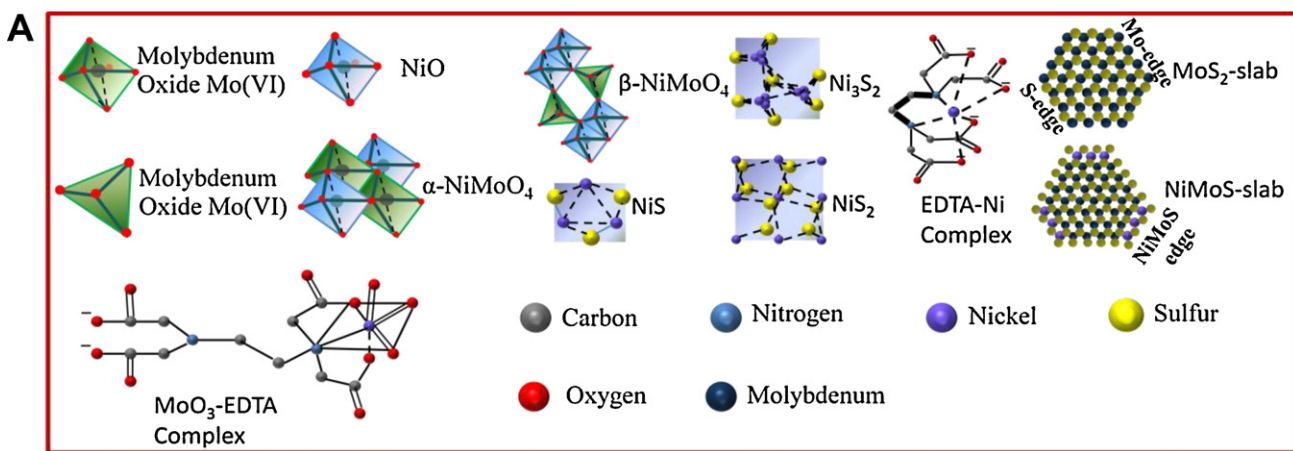
Scheme 2B represents the sulfidation mechanism and structure of active phase for CAT 1. In oxide state of CAT 1, MoO₃ is present in lumps and average MoO₃ crystallite size is around 25 nm which

is one order magnitude higher than that of SBA-15 pore size. Thus, a fraction of MoO₃ crystallites stay on the external surface of silica SBA-15 as shown in schematic for CAT 1 oxide (see Scheme 2B). It indicates the poor dispersion of MoO₃. Also, most of the nickel is present in EDTA–Ni complex. Ni usually helps in better dispersion of molybdenum oxide because of its electron donating nature as discussed in Section 3.4 for Raman analysis and also shown by Gutierrez et al. [45]. In CAT 1 only small amount of Ni is in oxide state and most of the Ni is in complex with EDTA and does not participate in dispersion of MoO₃ causing the formation of large MoO₃ crystallites. XRD and RAMAN analyses also present the same conclusion. During sulfidation at temperature of 150 °C NiO converts to nickel sulfide and EDTA–Ni complex remains stable. Large crystals of MoO₃ start to break into small crystals and most of MoO₃ present on the external surface of SBA-15 will migrate to inside the pores and lead to better dispersion. At sulfidation temperatures above 150 °C MoO₃ starts to sulfide as well as disperse better where as EDTA–Ni complex is still stable. As shown in Scheme 2B at sulfidation temperature of 220 °C EDTA–Ni complex breaks down releasing the Ni atoms, these Ni atoms help to further improve the dispersion of molybdenum. Ni atoms then sit on the corners and edges of MoS₂ slabs and then while on the edge and corner these Ni atoms also get sulfided and results in the formation of NiMoS active phase as shown in CAT 1 sulfide at 250 °C in Scheme 2B.

Further increase in temperature to 350 °C leads to the complete sulfidation and better dispersion of Ni and Mo, and also helps in formation of fully sulfided Ni–Mo–S multilayer type II active phases which results in better activity of CAT 1 over CAT 0 as shown in Table 4. The CO chemisorptions data (Table 2) show that under these conditions the average crystal size is 8.7 nm which is much lower as compared to 25 nm in CAT 1 oxide. This signifies the better molybdenum dispersion. As the average crystal size (8.7 nm) is more than the pore size of SBA-15, a fraction of molybdenum oxide is present on the external surface of SBA-15. During sulfidation, at 350 °C these will also sulfide on external surface and that may produce randomly oriented MoS₂ slabs (see Fig. 15C). EDTA thus helps in delaying the sulfidation of Ni to the point where molybdenum is already sulfided. This effect helps in the formation of more type II Ni–Mo–S active phase which results in better activity as compared to catalyst without chelating ligand.

It can be seen from HRTEM analysis Fig. 16 and Table 3 that number of layers were reduced from average value of 4.6 for CAT 0 to average value of 2.9 for CAT 1 and main reason can be explained as follows: in case of CAT 0 dispersion of MoO₃ is better as compared to CAT 1 and CAT 2 (XRD and Raman, Sections 3.2 and 3.4) because Ni improves the dispersion MoO₃ in oxide state in CAT 0 but Ni converts to nickel sulfide at 150 °C, which implies that no nickel is available to improve the dispersion at higher temperature zone where multiple stacking of MoS₂ happens and leads to higher stacking order and length of MoS₂ layers in CAT 0. In oxide state of CAT 1 lumps of MoO₃ crystals were formed as most of the Ni is in complex with EDTA. But at temperatures above 220 °C EDTA–Ni complex decomposes leaving behind Ni which helps in better dispersion of Mo at higher temperature zone where multiple of stacking MoS₂ occurs leading to lower average stacking order and length.

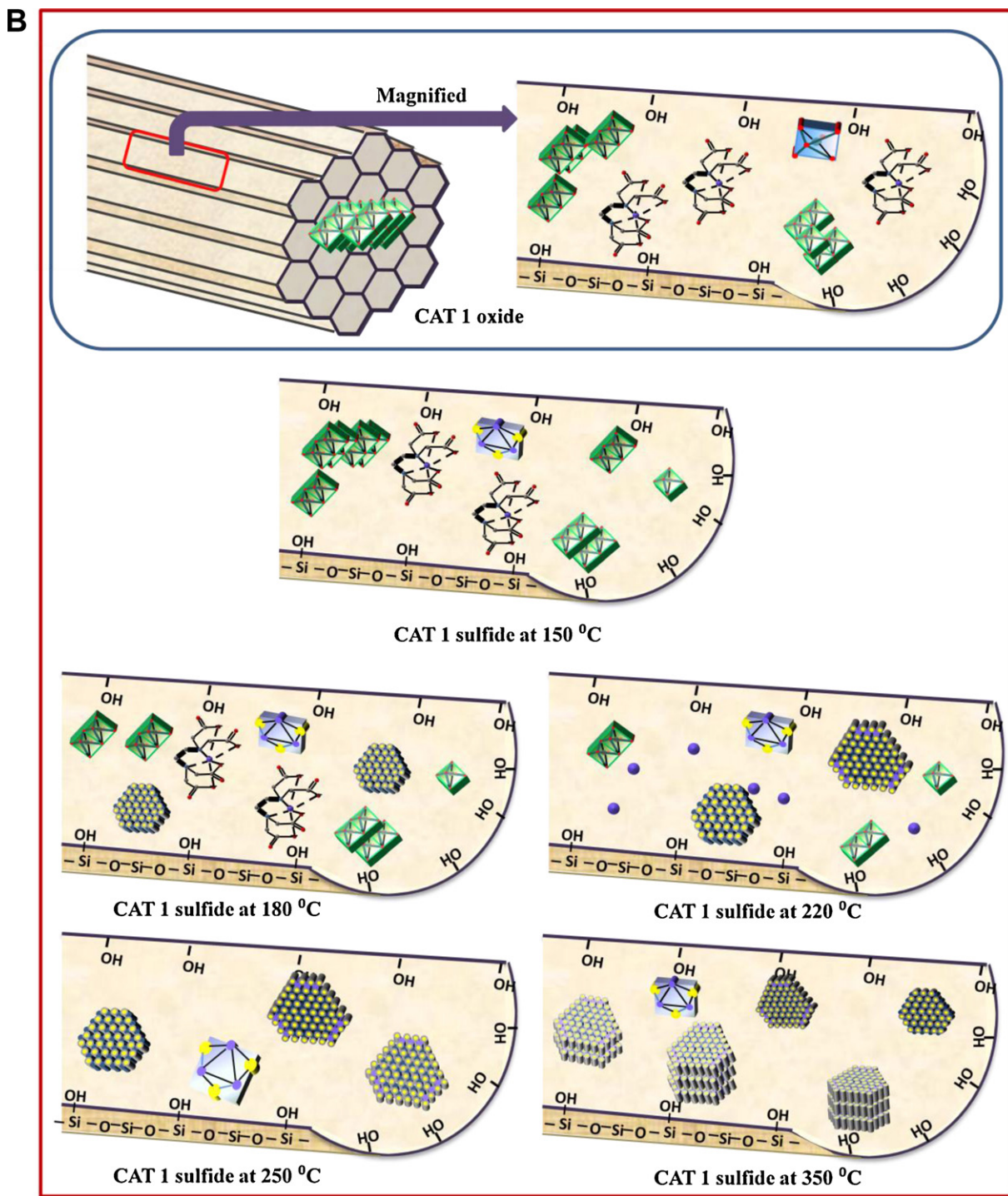
The sulfidation mechanism and genesis of active phase in CAT 2 is represented in Scheme 2C. CAT 2 has twice EDTA concentration as compared to CAT 1 which implies that almost all Ni forms complex with EDTA. Similar to as in case of CAT 1, there is formation of large MoO₃ crystallites (~25 nm) which are present on the external surface of silica SBA-15. Excess EDTA interacts with support via OH group as shown in Scheme 2C for CAT 2 oxide and as well as it forms [(MoO₃)₂EDTA] complex with Mo, the same is shown by TPR profile of CAT 2 in Section 3.6. The interaction of EDTA with surface hydroxyl groups also reduces the number of available hydroxyl groups for MoO₃ to interact, leading to the formation of more lumps



Scheme 2. Sulfidation mechanism.

of MoO_3 crystallites in oxide state as compared to CAT 1 as shown in Scheme 2B and C. During sulfidation, as explained in case of CAT 1, large crystals of MoO_3 start to break into small crystals at 150°C and tend to disperse better. With increase in sulfidation temperature above 150°C molybdenum starts to sulfide and at 220°C EDTA–Ni complex decomposes to release nickel which then sits on the corners and edge of MoS_2 slab to form NiMoS active phase as shown in

Scheme 2C for CAT2 sulfide at 250 °C. Further increase in sulfidation temperature to 350 °C helps in the complete sulfidation of molybdenum and as well as of nickel which is present on the corners and edges of MoS₂ slab. Also the increase in temperature helps in the multiple stacking of MoS₂ slabs. At 350 °C there is formation of fully sulfidized, two to three layered, type II Ni–Mo–S active phase. The CO chemisorption data (Table 2) show that under similar reduction



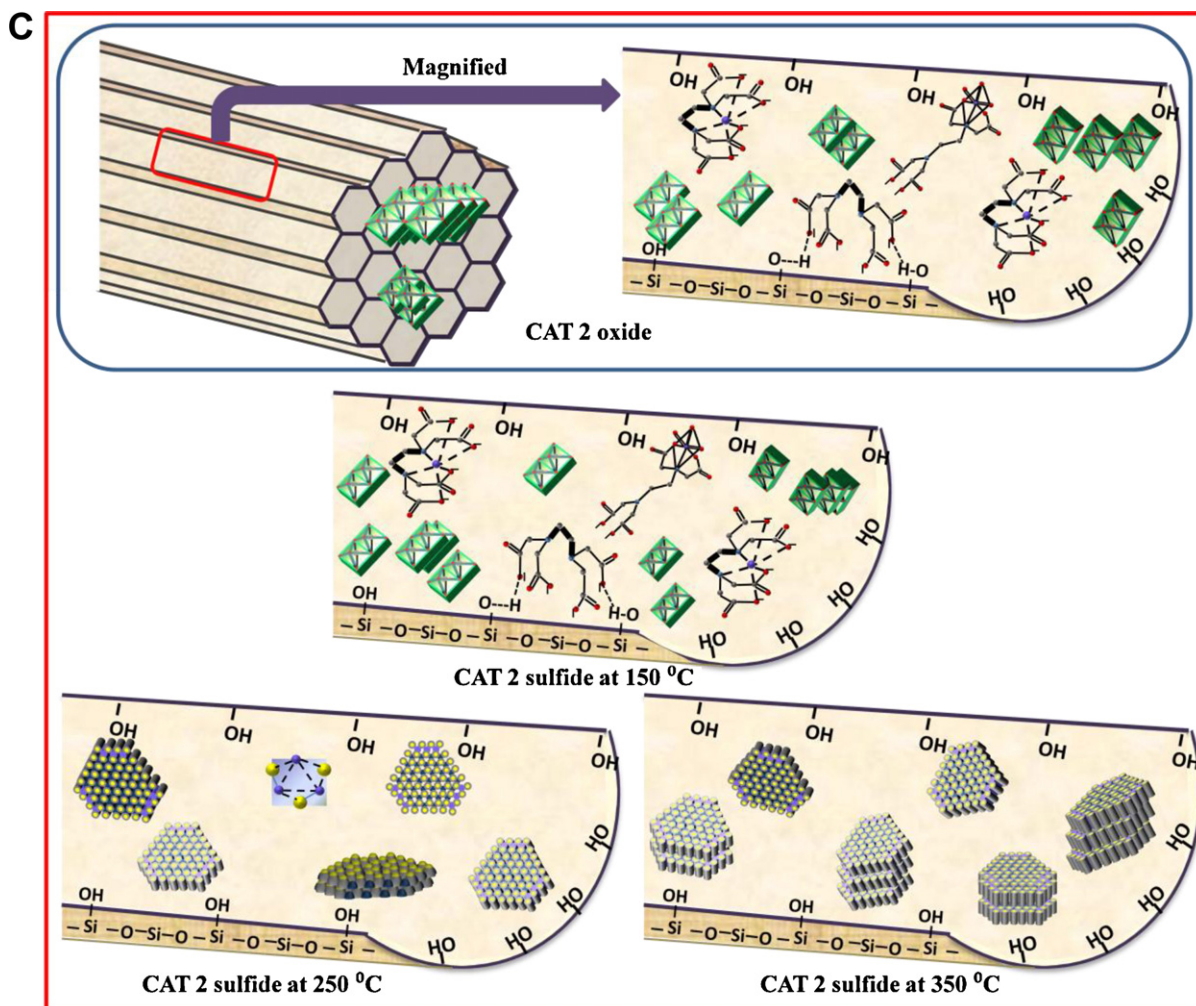
Scheme 2. (Continued)

conditions the average crystal size reduces to 6.5 nm from 25 nm as in case of CAT 2 oxide. This average crystal size (6.5 nm) is less than the pore size of SBA-15. It signifies that most of the molybdenum migrate to inside the ordered pore structure of SBA-15. Thus MoS₂ slabs for CAT 2 appear to be ordered as compared to CAT 1 (see Fig. 15C and D).

The activity of CAT 2 is more as compared to CAT 1 because the numbers of Type-II Ni–Mo–S active phases are less in CAT 1 as compared to CAT 2 as shown in Scheme 2B and C for CAT 1 and CAT 2 sulfided at 350 °C. The main reason is that in CAT 2 quantity of EDTA is more which results in encapsulation of almost all of the

nickel present. Therefore, the amount of nickel released at 220 °C in CAT 2 is more than that of CAT 1 resulting in availability of more of Ni atoms which leads to (i) better dispersion of Mo at higher temperature zone where multiple of stacking MoS₂ occurs leading to lower average stacking order and length as compared to CAT 1 and (ii) availability of more Ni atoms to sit on the corners and edges of MoS₂ slab to form more numbers of NiMoS active phases.

From the above discussion it can be concluded that all the characterization results are well correlating with catalytic activity. It is clear from above discussion that increase in EDTA helps to increase in activity, although EDTA to Ni molar ratio of 3, 4 and 5 and



Scheme 2. (Continued)

corresponding catalysts also have been tried to get optimum EDTA/Ni ratio and these catalysts are named as CAT 3, CAT 4 and CAT 5. All these catalysts were screened with LGO and the activity results are shown in Table 4. It is clear from Table 4 that the hydrotreating activity increases with EDTA loading up to 4 EDTA and then starts to decrease because excess EDTA will block the pores and this result in reduction of available surface area.

4. Conclusions

In the present work, a series of NiMo catalysts supported on SBA-15 with different EDTA/Ni molar ratio were prepared. A beneficial effect of chelating agent was seen when the sulfided catalysts were tested in the light gas oil hydrotreating. Characterization by XANES pointed out the delayed Ni^{2+} sulfidation (to the temperatures where molybdenum already started to sulfide) as the main cause of improvement in HDS and HDN activity of the catalysts prepared in presence of organic chelates. Nickel sulfidation starts when the EDTA complex decomposes. As a result, nickel atoms released by the chelating agent can move to the reactive edges of the MoS_2 to form a finely dispersed sulfide $\text{Ni}–\text{Mo}–\text{S}$ type II active phase. It was clear from XRD and RAMAN analyses that with increase in EDTA/Ni molar ratio, the amount of Ni available to aid molybdenum dispersion decreases and the size of MoO_3 crystallites increases, leading to poor dispersion. During sulfidation, released Ni helps in better dispersion of Mo species and there is significant reduction in length

and stacking of MoS_2 with maximum reduction in CAT 2 and minimum in CAT 0. This is confirmed by HRTEM and CO chemisorption analysis results. FTIR results indicate the interaction of EDTA with support via surface OH groups leading to weak metal support interactions. It favors the formation of large MoO_3 crystallites, which are then easy to sulfide. Activity studies have shown that, for catalyst CAT 4 there is 28% increase in HDS of LGO as compared to $\text{NiMo}/\gamma\text{-Al}_2\text{O}_3$. HDN conversions for $\text{NiMo}/\gamma\text{-Al}_2\text{O}_3$ are better than for $\text{NiMo}/\text{SBA-15}$ and are almost equal with the catalyst containing EDTA/Ni molar ratio of 4. This may be because of weak acidity of SBA-15 support as compared to that of γ -alumina support.

Acknowledgments

The authors are grateful to Syncrude Canada Ltd., Natural Sciences and Engineering Research Council of Canada for financial support and Canadian Light Source for providing the facility of XANES analysis for this research.

References

- [1] Y. Okamoto, M. Breysse, G.M. Dhar, C. Song, *Catalysis Today* 86 (2003) 1–4.
- [2] C. Song, *Catalysis Today* 86 (2003) 211–263.
- [3] N. Rinaldi, T. Kubota, Y. Okamoto, *Applied Catalysis A: General* 374 (2010) 228–236.
- [4] T.K.T. Ninh, L. Massin, D. Laurenti, M. Vrinat, *Applied Catalysis A: General* 407 (2011) 29–39.
- [5] M. Sun, D. Nicosia, R. Prins, *Catalysis Today* 86 (2003) 173–189.

- [6] M. Breysse, P. Afanasiev, C. Geantet, M. Vrinat, *Catalysis Today* 86 (2003) 5–16.
- [7] P.E. Boahene, K. Soni, A.K. Dalai, J. Adjaye, *Applied Catalysis B: Environmental* 101 (2011) 294–305.
- [8] N. Kunisada, K.H. Choi, Y. Korai, I. Mochida, K. Nakano, *Applied Catalysis A: General* 269 (2004) 43–51.
- [9] T. Klimova, J. Reyes, O. Gutierrez, L. Lizama, *Applied Catalysis* 335 (2008) 159–171.
- [10] J.C. Duchet, M.J. Tilliete, D. Cornet, L. Vivier, G. Perot, L. Bekakra, C. Moreau, G. Szabo, *Catalysis Today* 10 (1991) 579–592.
- [11] J. Ramirez, S. Fuentes, G. Diaz, M. Vrinat, M. Breysse, M. Lacroix, *Applied Catalysis* 52 (1989) 211–224.
- [12] A.C. Faro Jr., A.C.B. dos Santos, *Catalysis Today* 118 (2006) 402–409.
- [13] J. Escobar, M.C. Barrera, J.A.D. Reyes, J.A. Toledo, V. Santes, J.A. Colin, *Journal of Molecular Catalysis A* 287 (2008) 33–40.
- [14] L. Kaluza, M. Zdravil, *Collection of Czechoslovak Chemical Communications* 73 (2008) 945–955.
- [15] L. Ding, Y. Zheng, Z. Zhang, Z. Ring, J. Chen, *Journal of Catalysis* 241 (2006) 435.
- [16] G.M. Kumaran, S. Garg, K. Soni, V.V.D.N. Prasad, L.D. Sharma, G.M. Dhar, *Energy Fuels* 20 (2006) 1784–1790.
- [17] D. Trong On, D. Desplantier-Giscard, C. Danumah, S. Kaliaguine, *Applied Catalysis A: General* 253 (2003) 545–602.
- [18] C.S. Shalaby, S.K. Saha, X. Ma, C. Song, *Applied Catalysis B: Environmental* 101 (2011) 718–726.
- [19] K. Soni, P.E. Boahene, K. Chandra Mouli, A.K. Dalai, J. Adjaye, *Applied Catalysis A: General* 398 (2011) 27–36.
- [20] K.C. Mouli, K. Soni, A. Dalai, J. Adjaye, *Applied Catalysis A: General* 404 (2011) 21–29.
- [21] L. Vradman, M.V. Landau, M. Herskowitz, V. Ezersky, M. Talianka, S. Nikitenko, Y. Koltypin, A. Gedanken, *Journal of Catalysis* 213 (2003) 163–175.
- [22] T. Klimova, L. Lizama, J.C. Amezcua, P. Roquero, E. Terres, J. Navarrete, J.M. Dominguez, *Catalysis Today* 98 (2004) 141–150.
- [23] K. Soni, B.S. Rana, A.K. Sinha, A. Bhaumik, M. Nandi, M. Kumar, G.M. Dhar, *Applied Catalysis B: Environmental* 90 (2009) 55–63.
- [24] K. Soni, K.C. Mouli, A.K. Dalai, J. Adjaye, *Catalysis Letters* 136 (2010) 116–125.
- [25] S. Garg, T. Bhaskar, K. Soni, G.M. Kumaran, A. Muto, Y. Sakata, G. Murali Dhar, *Chemical Communications* 42 (2008) 5310–5311.
- [26] K. Soni, P.E. Boahene, A.K. Dalai, *ACS Symposium Series, Production and Purification of Ultraclean Transportation fuels*, 1088 (2011) 15–29.
- [27] P.E. Boahene, K. Soni, A.K. Dalai, J. Adjaye, *Applied Catalysis, B* 101 (2011) 294–305.
- [28] L. Vradman, M.V. Landau, M. Herskowitz, V. Ezersky, M. Talianker, S. Nikitenko, Y. Koltypin, A. Gedanken, *Journal of Catalysis* 213 (2003) 163–175.
- [29] G. Murali Dhar, G.M. Kumaran, M. Kumar, K.S. Rawat, L.D. Sharma, B.D. Raju, K.S. Rama Rao, *Catalysis Today* 99 (2005) 309–314.
- [30] M.S. Thompson, European Patent Application 0.181.035 (1986).
- [31] A. Stanislaus, A. Marafi, M.S. Rana, *Catalysis Today* 153 (2010) 1–68.
- [32] G. Kishan, L. Coulier, V.H.J. de Beer, J.A.R. van Veen, J.W. Niemantsverdriet, *Journal of Catalysis* 196 (2000) 180–189.
- [33] R. Cattaneo, T. Shido, R. Prins, *Journal of Catalysis* 185 (1999) 199–212.
- [34] M.S. Rana, J. Ramirez, A. Gutiérrez-Alejandre, J. Ancheyta, L. Cedeño, S.K. Maity, *Journal of Catalysis* 246 (2007) 100–108.
- [35] A.I. Dugulan, M.W.J. Crajé, G.J. Kearley, *Journal of Catalysis* 222 (2004) 281–284.
- [36] R. Cattaneo, T. Weber, T. Shido, R. Prins, *Journal of Catalysis* 191 (2000) 225–236.
- [37] R. Cattaneo, F. Rota, R. Prins, *Journal of Catalysis* 199 (2001) 318–327.
- [38] R. Cattaneo, T. Shido, R. Prins, *Journal of Synchrotron Radiation* 8 (2001) 158–162.
- [39] P. Blanchard, C. Mauchausse, E. Payen, J. Grimblot, *Studies in Surface Science and Catalysis* 91 (1995) 1037–1049.
- [40] E.J.M. Hensen, P.J. Kooyman, Y. van der Meer, A.M. van der Kraan, V.H.J. de Beer, J.A.R. van Veen, R.A. van Santen, *Journal of Catalysis* 199 (2001) 224–235.
- [41] Y. Okamoto, S.Y. Ishihara, M. Kawano, M. Satoh, T. Kubota, *Journal of Catalysis* 217 (2003) 12–22.
- [42] S.L. Gonzalez-Cortés, T.-C. Xiao, P.M.F.J. Costa, B. Fontal, M.L.H. Green, *Applied Catalysis A* 270 (2004) 209–222.
- [43] K. Hiroshima, T. Mochizuki, T. Homma, T. Shimizu, M. Yamada, *Applied Surface Science* 121/122 (1997) 433–436.
- [44] V. Sundaramurthy, A.K. Dalai, J. Adjaye, *Catalysis Letters* 102 (2005) 299.
- [45] B. Moreno, E. Chinarro, M.T. Colomer, J.R. Jurado, *Journal of Physical Chemistry C* 114 (2010) 4251–4257.
- [46] B.D. Cullity, *Elements of X-ray Diffraction*, 2nd ed., Addison-Wesley, Menlo Park, CA, 1978.
- [47] O.Y. Gutierrez, F. Perez, G.A. Fuentes, X. Bokhimi, T. Klimova, *Catalysis Today* 130 (2008) 292–301.
- [48] S. Oyama, T. Gott, K. Asakura, S. Takakusagi, K. Miyazaki, Y. Koike, K.K. Bando, *Journal of Catalysis* 268 (2009) 209–222.
- [49] P. Mazoyer, C. Geantet, F. Dieh, C. Pichon, T.S. Nguyen, M. Lacroix, *Oil & Gas Science and Technology* 60 (2005) 791.
- [50] F. Farges, G.E. Brown, J.J. Rehr, *Journal of Physical Review B* 56 (1997) 1809.
- [51] F.W. Lytle, R.B. Gregor, *Physical Review B* 37 (1988) 1550.
- [52] Hydrotreating Catalysts Preparation, Characterization and Performance, *Proceedings of the Annual International AIChE Meeting* vol. 50, pp. iii–x, 1–295 (1989).
- [53] J.A. Rodriguez, S. Chaturvedi, J.C. Hanson, *Journal of Physical Chemistry B* 102 (1998) 1347–1355.
- [54] S. Chaturvedi, J.A. Rodriguez, J.C. Hanson, *Catalysis Letters* 51 (1998) 85–93.
- [55] C.A. Muryn, D. Purdie, P. Hardman, A.L. Johnson, N.S. Prakash, S. Ganesh, N. Raiker, G. Thornton, *Faraday Discussions of the Chemical Society* 89 (1990) 77–89.
- [56] P. Biswas, P. Narayanasarma, K.C. Mouli, A.K. Dalai, J. Adjaye, *Industrial and Engineering Chemistry Research* 50 (2011) 7835–7882.
- [57] P. Rayo, M.S. Rana, J. Ramirez, J. Ancheyta, A.A. Elguezabal, *Catalysis Today* 130 (2008) 283–291.
- [58] R. Nava, R.A. Ortega, G. Alonso, C. Ornelas, B. Pawelec, J.L.G. Fierro, *Catalysis Today* 127 (2007) 70–84.
- [59] X. Wang, P. Wang, Z. Dong, Z. Dong, Z. Ma, J. Jiang, R. Li, J. Ma, *Nanoscale Research Letters* 5 (2010) 1468–1473.
- [60] J. Ryczkowski, *Catalysis Today* 68 (2001) 263–381.
- [61] J. Ryczkowski, *Vibrational Spectroscopy* 22 (2000) 55–62.
- [62] J. Ryczkowski, *Applied Surface Science* 252 (2005) 813–822.
- [63] R.J. Kula, *Analytical Chemistry* 38 (1966) 1581–1584.
- [64] D. Ferdous, N.N. Bakhshi, A.K. Dalai, J. Adjaye, *Applied Catalysis, B* 72 (2007) 118–128.
- [65] Y. Li, D. Pan, C. Yu, Y. Fan, X. Bao, *Journal of Catalysis* 286 (2012) 124–136.
- [66] M.J. Girgis, B.C. Gates, *Industrial and Engineering Chemistry Research* 30 (1991) 2021–2058.
- [67] K. Al-Dalama, A. Stanislaus, *Energy & Fuels* 20 (2006) 1777–1783.